A preparation sequence for multi-analysis of μm-sized extraterrestrial and geological samples

Alice Aléon-toppani, Rosario Brunetto, Jérôme Aléon, Zelia Dionnet, Stefano Rubino, Dan Levy, David Troadec, François Brisset, Ferenc Borondics, Andrew King

A preparation sequence for multi-analysis of µm-sized extraterrestrial and geological samples

Alice Aléon-Toppani[1*], Rosario Brunetto[1], Jérôme Aléon[2], Zelia Dionnet[1,3,4], Stefano Rubino[1], Dan Levy[1,2], David Troadec[5], François Brisset[6], Ferenc Borondics[7], Andrew King[7]

1 - Institut d'Astrophysique Spatiale, UMR 8617, CNRS, Univ. Paris-Saclay, Bât 120-121, 91405 Orsay cedex, France
2 - Institut de Minéralogie, de Physique des Matériaux et de Cosmochimie, UMR 7590, Sorbonne Université, Museum National d'Histoire Naturelle, CNRS, IRD, 61 rue Buffon, 75005 Paris, France
3 - INAF-IAPS, Roma, Italy
4 - DIST-Università Parthenope, Napoli, Italy
5- Institut d'électronique de microélectronique et de nanotechnologie, UMR 8520, Laboratoire central, Cité scientifique, Avenue Henri Poincaré, CS 60069, 59652 Villeneuve d'Ascq cedex.
6- ICMMO, CNRS UMR 8182, Univ. Paris-Saclay, Orsay, France
7- SOLEIL synchrotron, Gif-sur-Yvette, France

*Corresponding author : alice.aleon@universite-paris-saclay.fr

Submitted to Meteoritics and Planetary Science- November 2020

Abstract (226 WORDS)

With the recent and on-going sample return missions and/or the developments of nano- to micro-scale 3D and 2D analytical techniques, it is necessary to develop sample preparation and analysis protocols that allow combination of different nanometer to micrometer scale resolution techniques and both maximize scientific outcome and minimize sample loss and contamination. Here, we present novel sample preparation and analytical procedures to extract a maximum of sub-micrometer structural, mineralogical, chemical, molecular and isotopic information from micrometric heterogeneous samples. The sample protocol goes from a non-destructive infrared (IR) tomography of ~10 to ~70 micrometer-size single grains, which provides the distribution and qualitative abundances of both mineral and organic phases, followed by its cutting in several slices at selected sites of interest for 2D mineralogical analysis (e.g. Transmission Electron Microscopy), molecular organic and

mineral analysis (e.g. Raman and/or IR micro-spectroscopy) and isotopic/chemical analysis (e.g. NanoSIMS). We also discuss here the importance of the focused ion beam microscopy in the protocol, the problems of sample loss and contamination and at last the possibility of combining successive different analyses in various orders on the same micrometric sample. Special care was notably taken to establish a protocol allowing correlated NanoSIMS/TEM/IR analyses with NanoSIMS performed first. Finally, we emphasize the interest of 3D and 2D IR analysis in studying the organics-minerals relationship in combination with more classical isotopic and mineralogical grain characterizations.

1. Introduction

Since the past few decades, analyses of microscopic samples have become increasingly important to extract a wealth of scientific information from rare and precious samples. On one hand, samples, such as the asteroid dust that will be returned by the Hayabusa2 (Watanabe et al., 2017, 2019, Jaumann et al., 2019) or the OSIRIX-REx (Hamilton et al., 2019, Lauretta et al., 2019) space missions, are expected to be very heterogeneous (close to carbonaceous chondrite mineralogy) and require analyses with techniques having nanometer scale resolution. On the other hand, to gain information from sample such as meteorites, geological or biological samples, processes are now increasingly examined at micro/nanometric scales with the aim of combining different in-situ complementary methods (e.g., Transmission Electron Microscopy (TEM) for mineralogy and chemical composition, InfraRed (IR) spectroscopy for molecular information on silicate and organic matter, Nanometer-scale Secondary Ion Mass Spectrometry (NanoSIMS) for isotopes).

In this context, it is necessary to perform multiple complementary analyses on micrometer-sized samples, from the least destructive to the most destructive methods to maximize scientific outcome and minimize sample loss and contamination. Multi-analytical sequences were successfully used in the recent past to analyze 1/ samples from comet Wild 2 and asteroid Itokawa returned by the Stardust and Hayabusa space missions, respectively (e.g., Nakamura et al., 2011, Zolensky et al., 2008) and 2/ very small and unique meteorites (e.g., Acfer 094, Matsumoto et al., 2019). Those sequences either consisted of successive analyses on the same thin section such as XANES (X-ray Absorption Near Edge Structure), TEM and finally NanoSIMS which, in the end, consumed integrally the section (e.g., Stadermann et al. 2005, Zolensky et al., 2008, De Gregorio et al., 2011), or consisted of 3D-XCT (X-ray Computed Tomography), -XRD (X-ray Diffraction) or -XRF (X-ray Fluorescence) analyses of a grain subsequently sliced in several sections, which were analyzed independently by different techniques (e.g., TEM or NanoSIMS, Nakamura et al., 2011, Matsumoto et al., 2019). Recent approaches to address this issue were to develop specific sample holders allowing multi-analyses (Ito et al., 2020) with limited contamination (Uesugi

et al., 2020, Shirai et al. 2020) or to increase the number of prepared samples from a single grain (e.g. Berger and Keller, 2015). However, none of these sequences allowed multi-analyses on the same section in variable order or reanalysis after the sequence was completed.

Here we present a novel sequence to analyze samples of ~10 to 70 µm-sized grains (Aléon-Toppani et al., 2020, Brunetto et al., 2020), which aims 1/ at maximizing the scientific output from a single grain and 2/ at combining different techniques on the same sample preparation step and 3/ at using the same technique at successive preparation steps to optimize the scientific information obtained from the sample. This sample analysis sequence begins by an innovative sample preparation of grains welded at the end of a holder needle. Special care is taken during sample preparation to minimize sample loss and sample contamination. Infrared computed micro-tomography (IR-CT) is performed as a first step for a non-destructive characterization of the 3D structure and chemistry of the grain (Dionnet et al., 2020). This notably allows identification of sub-regions of interest, which can be targeted for further analyses. Subsequently, we follow two different approaches: 1/ preparation of sequential focused ion beam (FIB) sections of single ~10 to 65 µm grains, for different 2D analytical methods (e.g., IR micro-spectroscopy, TEM, or NanoSIMS), and 2/ development of a new FIB section mounting protocol that allows a combination of different analytical methods on the same FIB section starting with NanoSIMS, followed by IR spectroscopy and/or TEM. The second approach can also be used on thick FIB sections extracted from polished sections that were preliminarily characterized by SEM (Scanning Electron Microscope). Here, we focus on 1/ IR imaging micro-spectroscopy because, in addition to being totally non-destructive and comparable to remote sensing observations of small bodies, it allows the possibility to detect and study the spatial distribution of molecular bonds associated to minerals, water and organic compounds and their co-localization, 2/ TEM as it allows the study at the atomic scale of the chemistry and the crystallographic structure of the particle and 3/ NanoSIMS as it provides the distribution of isotopes and trace elements at the 100 nm scale.

2. Materials and methods

2.1 Sample description

Reference minerals used in this study included San Carlos olivine, calcite, macusanite glass and two samples widely used for the analysis of water content and D/H ratios (the Bamble Mg-hastingsite amphibole (Engrand et al., 1999) and a mica (CRPG phlogopite, Govindaraju, 1994)). In the context of the sample return missions Hayabusa2 and OSIRIS-REx from carbonaceous asteroids, we also focused on carbonaceous chondrite samples. We prepared and analyzed single 10 to 70 µm sized grains extracted from the

Paris CM chondrite (Hewins et al., 2014) and from the NWA 5515 CK chondrite (Weisberg et al., 2009).

2.2. Sample preparation

As the first step of the preparation chain, the sample was deposited as a single grain on a conductive substrate. Two types of substrates were used: ultraclean silicon wafer and gold plates additionally cleaned with pure analysis-grade ethanol in an ultrasonic bath. Grains with size ranging from 5*40*20 to 97*53*40 µm were deposited on those substrates in an ISO 6 clean room. Owing to electrostatic bonds, they usually did not move from the substrate during the transport of the plate from the clean room to the FIB. However, these electrostatic bonds are not strong enough if the particle size exceeds ~70/100 µm. In this case, particles have to be directly handled in the FIB laboratory and deposited on the conductive substrate just before being inserted into the FIB chamber.
In addition, a few FIB sections extracted from polished sections of grains embedded in epoxy were used for the development of analytical techniques coupling.

2.3. Infrared and Raman micro-spectroscopy

Both IR and Raman micro-spectroscopy were performed at the SMIS beam-line of synchrotron SOLEIL (France). An Agilent Cary 670 Fourier-Transform IR microscope equipped with a Focal Plane Array Detector (FPA) was used for the IR characterization of the samples. The spectral resolution was either 4 or 8 cm^{-1}. The spectral range extended from 850 cm^{-1} to 3950 cm^{-1}. A 25× objective was used in combination with a high magnification system placed in front of the 128×128 pixels FPA detector. The projected pixel size was ~0.66 µm and the field of view was ~84 µm. The spatial resolution was diffraction-limited in the whole spectral range. Sections were analyzed in transmission mode. Acquisition time was limited to 128 or 256 scans. Before each analysis, a background spectrum was acquired. In addition, some of the IR analyses presented here were performed with a Thermo Continuum microscope coupled to a Thermo Nicolet 8700 FTIR spectrometer (Thermo Fisher) operating in transmission mode. The source was either the internal globar or the external synchrotron light source, which provides a 100-1000x higher brightness than the globar source.

Raman spectroscopy was also used as a complementary method to study the characteristics on the organic/carbonaceous matter. It was performed using a DXR Raman micro-spectrometer from Thermo Fisher with a 532 nm exciting laser radiation. Raman maps were recorded with a spectral resolution of 4 cm^{-1} and a spatial resolution of about 1 µm. The laser power was typically in the 0.2-0.5 mW range (conditions similar to what was used by Dionnet et al., 2018, on the Paris meteorite to avoid heating of the samples).

2.4. Nanoscale Secondary Ion Mass Spectrometry

NanoSIMS is a mass spectrometric method optimized for the scanning imaging of isotopes in µm-sized samples with a sub-µm spatial resolution given by the size of the primary ion beam. For some specific applications requiring efficient detection of trace isotopes (e.g. deuterium), intense primary beams with size on the order of 1 µm can also be used. Isotopic characterization was performed using the NanoSIMS 50 at IMPMC (Paris).

Amphibole and mica samples were studied using the protocol specifically developed to measure D/H ratios in FIB sections (Lévy et al. 2019). All samples were coated with 20 nm Au to ensure conductivity and measured after a storage time of 3 weeks in the vessel chamber of the instrument to ensure minimal residual surface contamination (Levy et al. 2019). The D/H analysis was performed using a 100 pA Cs^+ beam of ~1.5 µm in size, rastered over a 8 x 8 µm area. The dwell time was fixed to 1000 µs/pixel and images consist of 256 × 256 pixels. A Cs^+ preimplantation was performed during 8 min with a 250 pA beam rastered over 20 x 20 µm to remove Au coating and achieve sputtering equilibrium (hereafter presputtering). These analytical conditions correspond to optimal conditions for the measurement of D/H ratios on FIB sections as determined in Levy et al. (2019) and ensure a large degree of overlapping from pixel to pixel, which eliminates isotopic effects due to dynamic contamination during analysis and pitting effects during presputtering. Charging effects were compensated using the normal incidence electron gun. Negative secondary ions H^- and D^- were detected simultaneously using two electron multipliers. 20 image planes were acquired with typical count rates of ~1.5 x 10^5 counts per second (c/s) for H^- and ~10 c/s for D^- resulting in typical uncertainties of ~20‰ at the FIB section scale. H isotopic compositions are reported as δD deviations relative to the Standard Mean Ocean Water reference (SMOW, D/H_{SMOW} = 1.5576 x 10^{-4}) given in‰, where $\delta D = (D/H_{sample} / D/H_{SMOW} - 1) \times 1000$.

2.5. Transmission electron microscopy

Transmission electron microscopy is an electron based imaging technique with atomic resolution that gives access to the sub-µm structure of the sample, and to information about the crystallography and chemical composition of the minerals/phases constituting the sample. Samples were characterized using a 200 kV FEI field emission transmission microscope (IMPMC, Paris) and a 200 kV 2100+ JEOL microscope (Univ. Paris-Saclay). Both microscopes were equipped with high angle annular dark field detector and EDS energy-dispersive spectrometer.

Imaging was carried out in a conventional mode (bright field) as well as in scanning mode using the high angle annular dark field (HAADF) detector. A few chemical analyses were obtained in the conventional mode. Imaging and EDS were carried out with low dose conditions to minimize sample damage. Element abundances acquired on a SAMx IDFix system were quantified from EDS spectra by fitting peaks for all elements detected and applying a Cliff–Lorimer thin-film correction procedure (Cliff and Lorimer, 1975). The typical precision is about 10%. Elemental abundances were normalized to 100%.

2.6. Scanning electron microscopy (SEM)

Characterization of polished samples or sample topography was performed using a Zeiss Supra 55 VP FEG SEM (Univ. Paris-Saclay) equipped with an EDAX energy dispersive detector.

2.7. Focused ion beam technique

Samples were prepared using a FEI Strata DB 235 SEM-FIB microscope at IEMN (Lille). It was used to (1) weld the single grains at the tip of W needles to perform X-ray and IR micro-tomography, (2) recover the grains from the W needle and deposit them on a conductive substrate in order to cut them in several slices of different thickness. After extraction, the slices were either welded on TEM grids for 2D-IR spectroscopy and TEM characterization, or mounted on Al disk for NanoSIMS characterization. For NanoSIMS analyses, the sample slices were sometimes directly extracted from samples embedded in epoxy, polished and carbon or gold coated.

During FIB sample preparation, a focused beam of gallium ions was used either to ablate volumes of solids in precise locations and at carefully controlled rates with tolerances as fine as ~100 nm or to crack the organo-Pt gas to make precise welding. The samples can be imaged at micrometer resolution during preparation using both secondary ions and electrons. Details of preparation are given in the results section.

3. Results

Here, we present 1/ the non-destructive 3D tomography of single µm-sized meteoritic grains and the associated preparation, 2/ the preparation of sequential FIB sections of the same single grain for different 2D analytical methods (e.g. IR, TEM or NanoSIMS) and 3/ a new FIB section mounting protocol that allows different analytical methods on the same FIB section starting with NanoSIMS.

3.1 3D micro-tomography of single grains

3.1.1 Preparation of the grain: FIB welding of a single grain at the tip of a needle

In order to perform 3D tomography of a micron-sized grain, it is necessary that the grain 1/ stays in sight for most of its surface and 2/ that it can rotate over 360°. The grain needs thus to be glued at the tip of a needle. In our study, a single grain deposited on a conductive substrate was welded with platinum or with SEM electronic glue (SEMGlue by Kleindiek Nanotechnik GmbH, Kleindiek et al, 2008; Martina et al., 2016) on a tungsten needle holder using the FIB (Fig. 1). An Al-needle was also successfully used. SEMGlue is an electron-beam hardening glue. Both types of welding were tested because each one has its own advantages: using e-glue prevents the deposition of high atomic number elements such as Pt (thus allowing some types of analyses such as XRF) whereas using Pt instead of e-glue or classical epoxy prevents the contamination of the extraterrestrial grain by terrestrial organics. For both types of welding, the FIB micro-manipulator needle was used as holder needle. In the case of a platinum welding, the holder needle approaches the grain with a tilt between 30° to 40° and gently touches the grain on a selected side. Pt is then carefully deposited at the contact between the grain and the tip of the W needle on a restricted surface using the ion beam (30 kV, 300 pA). Four welding points are usually made by rotating the needle at 0, 90, 180 and 270° to ensure a strong welding. In the case of the electronic glue welding, the W needle tip is dipped into the glue while it is still liquid and is subsequently approached to the grain. The electron beam is then used to polymerize the e-glue at the precise location of the contact between the grain and the tip of the needle. In both cases, the particle is initially deposited on the conductive substrate and holds only by electrostatic bonds. Once the welding is complete, the particle can thus be lifted using the W needle, which is finally removed from the FIB chamber.

As studied samples could contain extraterrestrial organic matter, it was important to check the carbon/organic contamination due to our preparation. In the case of the Pt welding, as an organo-Pt gas was used, a slight carbon deposition could be expected over the whole grain, or at least concentrated around the welding point. In the case of e-glue, glue could be a source of carbon contamination by itself. Here, we show that the degree of carbon contamination in the welding process is limited in spatial distribution and amount (Fig. 2 and 3). Indeed, as shown in Fig.1, both glue and Pt are spatially restricted to the welding zone.

In the case of Pt-glue, IR spectroscopy did not reveal the presence of any CH bonds from a carbon-contaminant layer on the grain, which would suggest an upper limit for the thickness of such a layer of few tens of nm. The presence of an aromatic contaminant was investigated by Raman micro-spectroscopy (Fig. 2). Figure 2 shows Raman analyses of carbon contamination for Pt-glue. A very weak dehydrogenated amorphous carbon Raman signature (large band at ~1500-1560 cm^{-1} and a shoulder around 1350 cm^{-1}) was detected around the Pt-welding at the interface between the sample and the needle, clearly

distinguishable both spectrally and spatially from the Raman signature of the poly-aromatic carbon of the meteorite (classical D and G bands, with the G band of the Paris meteorite peaking around 1590-1600 cm-1, e.g., Noun et al., 2019). The IR spectrum of the contact between a meteorite grain and the Pt welding confirms the presence of only amorphous dehydrogenated carbon when contamination is present (band around 1600 cm^{-1}). In the case of the Pt-welding, this difference evidences the presence of carbon contamination only near the welding point within about 5 µm (Fig 2b).

In the case of the e-glue, we have investigated the IR signatures of both the e-glue and the typical organic matter of the CM Paris meteorite. Their IR spectra between 1200 and 1800 cm^{-1} (Fig. 3) carry two distinct signatures: the e-glue presents a maximum around 1711 cm^{-1} (probably due to C=O stretching), while the indigenous organic matter has a maximum around 1603 cm^{-1} (probably -OH bending) with a much weaker band at ~1700 cm^{-1}. The distinct spatial distribution of the intensity of these two bands, plotted in Fig. 3, shows that the e-glue is concentrated around the transition area between the needle and the sample and does not contaminate the sample. In agreement with the IR signature, no clear Raman signature of poly-aromatic carbons was detected in the e-glue, but only a strong fluorescence signal (Fig 2a). This would allow an easy distinction between indigenous carbon and contamination if present.

For both the e-glue and Pt-welding, contamination is thus spatially restricted to the welding zone and shows a well-characterized spectral signature that could be easily distinguished from extraterrestrial organic matter.

41 grains of minerals or fragments of meteorites were welded following this procedure. 7.3% (3 grains) were lost during the welding process (e.g. cracks in the grains, deposition mistakes), 12.2% (5 grains) were lost during transport, 9.7% (4 grains) due to wrong handling. 23 grains were welded with Pt and 16 grains with e-glue. Over 70% of the grains (29 grains) were analyzed at least once. Among those 29 grains analyzed, 27% were lost after the first analyses and 73% were analyzed several times (e.g. IR or X micro-tomography). Losses after analyses were due to either handling errors or the detachment of the grain from the needle, which could be related to an increase in the fragility of the grains after harsh analysis such as high energy X-ray micro-tomography at different energies. After two to five campaigns of analyses, 34 % of these 29 grains are still available for further analyses. Overall, 51% of the grains were analyzed several times (up to 5 times) with different methods and 25% are still available for further characterization after one to 5 analyses. Thus a rather large proportion of grains survived multiple analyses, handling and transport. It must be emphasized that multiple analyses and handling of the grains induce numerous vibrations and shocks of various origin. For instance, during each campaign of analysis, the needle has to be fixed to a specific holder and can rotate up to 180 times in the

case of 3D analyses, suffering different types of vibration. Between each campaign of analyses, the grain fixed on the tip of the needle has to be placed back in a container to travel from one lab to another, suffering once again different vibrations. The survival of grains after analysis could thus be further increased by minimizing the transport of the grains between each analysis, using a facility to facility transport container or developing a universal sample holder that will prevent any handling of the needle (e.g. Ito et al., 2020). For most lost grains, SEM images show that the grains themselves broke rather than the welding (Supplementary Figure 1). To prevent grains loss from the needle, it is thus important to adjust the quantity and localization of Pt welding between the needle and the particle depending on its geometry or structure (e.g. presence of initial fracture, porous/non porous structure, presence of large welding surface…).

3.1.2. Example of 3D IR micro-tomography

Once a grain is mounted on a needle, it becomes available for 3D analytical methods, and different types of 3D characterization can be performed on the same single grain. As IR spectroscopy is a totally nondestructive method, we first performed IR micro-tomography with the Agilent Cary 670 IR microscope equipped with a FPA detector. The needle was connected to a motor to assure the rotation of the sample under the microscope, around the needle axis. Using the method described by Dionnet et al. (2020), we collected series of 2D hyper-spectral maps in transmission for 180 angles, which were later reconstructed to obtain the distribution of the different functional groups in 3D. The spectral resolution was 16 cm^{-1} for the 3D-IR tomography. We show here an example of 3D IR micro-tomography performed on a homogenous grain of calcite (Fig. 4). The continuum at 3550 cm^{-1}, shown in grey, is representative of all the matter (needle and sample). The reconstructed 3D distribution of the intensity of the 2500 $cm^{-}1$ calcite band is presented in red.

A complementary XCT measurement was performed at the PSICHE beam-line of SOLEIL with energy of 17.6 keV and a photon flux of $1.6x10^{11}$ phs/s/mm^2. XCT allowed us to study the morphology of the sample at a smaller scale. By combining the two techniques on the same sample, we used the better spatial resolution of the X-ray data to constrain the shape of the IR reconstruction and to partially compensate the scattering/diffraction effects visible on IR data (Dionnet et al., 2020). An example of a whole sequence in 3D, containing both IR tomography and XCT, has been performed on a fragment of NWA 5515 meteorite and will be presented in Section 4.1.

3.2. Sequential FIB preparation of single grains

3.2.1. Preparation of several sections from single grains

After IR-CT analyses, single grains can be recovered and sliced into several sections for further 2D mineralogical, chemical and isotopic analyses (Fig. 5). The holder needle is put back in the FIB chamber in place of the micromanipulator needle (Fig. 5a). Using the Ga beam of the FIB focused at the contact between the grain and the holder needle, the grain is removed from the needle and retrieved on a conductive substrate (Fig. 5b).

Small and very heterogeneous grains are completely covered by platinum in order to be protected from irradiation damages and to improve cohesion (Fig. 5c). The Ga beam is subsequently used to cut the grain into several slices (Fig. 5d,e). Then, one after the other, the slices are connected to the W needle using Pt and separated from the substrate using the Ga beam (Fig 5f). The grains usually have an irregular shapes and can be sliced perpendicular to their longest dimension. The width and the height of a grain which can be easily cut are limited to ~20 to ~30 microns as wide cuts would be required to create a cross section of larger particles and FIB sections larger than 20 to 30 microns would be difficult to manipulate.

In the example provided here, dedicated sections for IR and TEM analyses were welded to a TEM grid using Pt-deposition (Giannuzzi and Stevie, 1999; Heaney et al., 2001). Sections for TEM analysis were finally thinned in situ down to ~100 nm for electron beam transparency (Fig 5i) and sections for IR mapping were thinned down to 1 µm (Fig 5h). Both sections were cleaned using a low energy Ga beam at grazing incidence. Finally, one 3 µm-thick section was retrieved for NanoSIMS analyses and deposited on a Al substrate (see section 3.3. for details). Images of the FIB sections (Fig. 5g, h, i) show the grain rimmed by a layer of Pt previously deposited over the whole grain. A thin outer layer made of the conductive substrate material that was sputtered by the Ga beam during the cutting of the section from the substrate was sometimes present.

The ion beam current used during the process was chosen to minimize degradation of the FIB sections. Ion beam voltage was 30 kV except to finish the thinning of the section, which was performed at 5 kV to minimize the damages to the section. Intensities of the ion beam for the deposition of Pt were between 3 nA and 1 nA with a defocused beam. It was around 20 nA with a large diaphragm to 7 nA to trench the sides and the edges of the section and finally 3 to 1 nA to thin the section down to 1 µm and 300 to 500 pA to finish the thinning of the section. Under similar experimental conditions, fragile phases such as phyllosilicates, glass, or even organic material are usually left undamaged, suggesting that our final TEM sections were not damaged during their preparation (Heaney, 2001; Lee et al., 2003; Mayer et al, 2007). In addition, (1) using a low voltage during the final thinning, (2) transferring a much thicker liftout section (1 to 3 microns – Fig 5) to the TEM grid, (3)

minimizing the electron beam imaging during the thinning of the section, (4) lowering the ion beam overlap or creating a rigid Pt or natural frame around the thin section (see Fig. 5 or supplementary Fig. 4) increase the preservation of organic matter and minimize local specimen heating and mechanical failure (Bassin et al, 2012). If an Ar beam gun is available in the FIB, it could be used to remove the very thin damage layer formed during the Ga ion beam treatment (Kodama et al. 2020).

Thanks to this process, we were able to obtain 3 slices of about 3 µm thickness from a ~10×20 µm grain of olivine and 5 slices of 1 to 3 µm thickness from a ~35×35×15 µm grain of the NWA 5515 chondrite. The loss due to the ablation of the slice is estimated to be around 50%. It is noticeable that after analyses, the two largest slices could be recovered and thinned again to be observed with the TEM. Note that for large FIB section (over ~15 by ~15 microns), the thinning of the section can only be limited to the zones of interest.

3.2.2 Example of IR and Raman spectra of 2D sections

IR transmission micro-spectroscopy of a 700 nm thick FIB section extracted from a single grain of olivine was performed using the synchrotron beam with an aperture of 8×8 µm, a resolution of 8 cm^{-1} and summing 2048 scans. The Raman mapping was performed in conditions described in paragraph 2.3 with a resolution of 4 cm^{-1}.

The spectra (Fig. 6) show high quality IR and Raman signatures of olivine within the grain. The IR spectrum shows typical olivine peaks at ~838 cm^{-1}, ~875 cm^{-1}, 980 cm^{-1} (Hamilton, 2010) and a supplementary peak at 1050 cm^{-1} which could correspond to a weak band of olivine or more probably to amorphous silicate related to a slight re-deposition of oxidized substrate atoms. The Raman spectrum shows the typical olivine peaks at 822 cm^{-1} and 855-856 cm^{-1}. By contrast, the Pt rim shows presence of a large G band around 1530 cm^{-1} and a shoulder at 1350 cm^{-1} (D band) which can be attributed to the presence of amorphous carbon deposited together with the Pt, similarly to what described above. This amorphous carbon results from the cracking of the organo-metallic gas during Pt deposition. Note that in the absence of Pt deposition, we did not detect any signature of amorphous carbon (paragraph 3.1).

Our different test experiments indicate that a thickness around 1 to 2 µm is a correct thickness for transmission FTIR analysis, either with synchrotron or globar source. We have calculated that for a 700 nm thick section of macusanite glass, the signal to noise ratio is at least 4 times better with the synchrotron source than the globar source (Supplementary Figure 2). When looking at much thinner sections such as TEM sections (~100 nm), the signal/noise ratio is rather low even with the synchrotron, allowing only a first order analysis of the species present in the section.

As a slight re-deposition of substrate atoms could be expected during FIB preparation, care must be taken in the choice of the substrate. For example, a gold wafer must be used instead of a silicon wafer if the study of silicates is of importance, in order to avoid any deposition of amorphous silicon during FIB preparation.

3.3 Nanosims analyses of 2D thick sections and following TEM and IR analyses

3.3.1. Constraints of NanoSIMS analysis and preparation of the 2D sections

Ever since the development of NanoSIMS analyses, coupling with other microscopies or micro-spectrometries has been investigated for the analysis of small and precious samples (e.g. Nguyen et al. 2007, Matrajt et al. 2008, De Gregorio et al. 2011, Floss et al. 2014). However, NanoSIMS analyses are usually performed after all other analyses because they are destructive at the 100 nm scale. They can be performed on almost any flat sample surface, provided charge accumulation can be prevented. For instance, NanoSIMS has been done after TEM (e.g. Stadermann et al. 2005, Eswara et al. 2019 and refs within) or after TEM + STXM (Le Guillou et al. 2013). Performing NanoSIMS imaging last implies (1) that mineralogical/chemical analysis of the samples must be complete before trace elements/isotopes can be analyzed (e.g. Messenger et al. 2005) and (2) 100 nm-thick samples such as TEM sections are usually completely sputtered away after analysis or have suffered damages beyond the possibility of further analyses (e.g. Stadermann et al. 2005).
If NanoSIMS analyses are performed first (e.g. to detect isotopically anomalous components in extraterrestrial matter or experimental samples), two approaches have been developed up to now to characterize the phase(s) of interest (e.g. mineralogy of the carrier phase). (i) Sequential ultramicrotome sections have been prepared so that adjacent sections can be analyzed by different techniques (e.g. Simon et al. 2008, Matrajt et al. 2008, De Gregorio et al. 2011, Penen et al. 2016). (ii) Alternatively, a second FIB section has been extracted perpendicularly to the NanoSIMS analysis surface of the first FIB section (or the initial polished section or grain, Smith et al. 2005, Floss et al. 2014, Suer et al. 2017), which must be thick enough (Suer et al. 2017). This also has the disadvantage that the area of interest is in direct contact with the protective Pt coating deposited during the second FIB sectioning and may suffer contamination preventing clean EDS chemical analysis or high-resolution imaging.

Our new sample mounting procedure to perform NanoSIMS imaging of FIB sections before subsequent correlated analysis by synchrotron-based micro-spectroscopies and/or TEM has several requirements: (1) the section of interest must be thicker than the depth of NanoSIMS analysis, (2) distortion of field lines, charging and topography due to sample

preparation must be minimal for NanoSIMS analysis and (3) the atomic layers damaged by the ion beam must be removed before subsequent mineralogical analyzes.

To solve these issues, we prepared 2 to 3 µm thick FIB sections, which were deposited on flat conductive NanoSIMS sample mounts. We used Si wafers and polished Al or stainless steel disks and found that Al-disks were easier to produce, handle and adapt to the NanoSIMS sample holders so that they were used preferentially. The FIB sections should be deposited on top of the Al-disk so that the surface to be analyzed is parallel to the extraction lens (EOS) and the topography is restricted to the thickness of the FIB section. However, if the whole surface of the FIB section is in contact with the disk, it is almost impossible to recover the FIB sections. The FIB sections were thus mounted on 1-2 µm bridges made of Pt deposited in the FIB-SEM (Fig. 7 a-d). To do so, two parallel Pt stripes are deposited onto the sample mount at a distance of ~the FIB section length from each other, in the central portion of the Al-disk mount for NanoSIMS. Being welded to a W needle, the FIB section is put into contact with the Pt stripes. Extremities of the FIB sections are then welded to the Pt stripes to form a bridge and maintain the FIB section onto the stripes. The Pt contact between needle and FIB section is finally cut.

Thick FIB sections used here can either be 3-µm thick FIB slices from single grains prepared as described in § 3.2 or be directly extracted from bulk sample embedded in epoxy. In the latter case, FIB sections are prepared in a classical way. A 2 µm-thick, 3 µm-wide Pt-strap is deposited on the surface of the polished section to protect it from ion damage (amorphisation or ion implantation). This is followed by ion beam milling of trenches on both sides and cuts at the edges of the section to produce a ~1-2 µm thick section. The FIB section is then extracted from the bulk material by "welding" it using Pt deposition to a tungsten needle controlled by micro-manipulator and severing the final connection to the surrounding material using the ion beam. Compared to ultramicrotomy preparation, where only grains can be prepared for analysis of adjacent slices, the advantage of this method is that both small grains and large polished samples embedded in epoxy can be analyzed, which allows to preserve sample context.

3.3.2. Control of instrumental mass fractionation

In order to ensure that FIB section mounting and preparation did not introduce further isotopic effects (i.e. modify the instrumental mass fractionation), we measured H isotopes in three samples of the Bamble amphibole (Fig. 8). Because of the very large relative mass difference between H and D, hydrogen isotopes are very sensitive to all instrumental effects and can be considered as good sensor of such effects. Three analyses of Bamble samples prepared as (i) polished section, (ii) FIB section deposited on an Al-disk without Pt bridge

and (iii) FIB section deposited on an Al-disk with a Pt-bridge yielded D/H ratios identical within error, indicating that the preparation of the FIB section and mounting on Pt bridges did not introduce measurable isotopic effects.

3.3.3. Post-NanoSIMS recovery of FIB sections

For recovery, the FIB section is severed from the Pt bridge using the Ga beam completely at one end of the section and partially at the other end (Fig. 7 e-h) so that the section still holds onto the disk by a small amount of Pt. The needle is then approached to the FIB section and welded to the free extremity of the section. Once the welding is complete, the partially cut side of the section is completely severed, resulting in a section free from the mount. The cut section is slightly smaller than the initial section (Fig. 7 f). The needle is subsequently lifted and the section welded to a regular M or finger grid. The top surface of the FIB section is gently cleaned from the NanoSIMS damages using a low intensity Ga beam from 1 nA to 300 pA (Fig. 9). In order to keep the section's thickness compatible with sensitivity of FTIR, the thinning step is limited to the removal of the layer damaged by ion sputtering during NanoSIMS analysis, while for subsequent TEM analysis, the section is thinned down to 100 nm. In order to preserve the portion of the section immediately adjacent to the bottom of the NanoSIMS analysis crater, i.e. corresponding to the end of the NanoSIMS analysis, it is necessary to remove material on the opposite side of the section that was analyzed by NanoSIMS (Fig. 9).

3.3.4. NanoSIMS-FTIR-TEM characterization sequences

The complete analytical sequence has been tested on a sample of CRPG phlogopite (Fig. 10). A 2 µm thick FIB section was extracted from the phlogopite standard included in epoxy and subsequently deposited on Pt bridges in the center of a 1 cm diameter Al-disk for further recovery (Fig. 10a). The H^- distribution map and δD map (Fig. 10b) show distinctly the mica section and its protective Pt coating deposited during FIB section preparation. While the raw δD value of ~ -100‰ of the mica (i.e. uncorrected from instrumental mass fraction) is well within typical raw compositions of natural terrestrial hydroxylated minerals measured in these conditions (Levy et al. 2019), the δD value of organometallic bonded H in Pt is much more negative (δD ~-500‰), which can be attributed to matrix effects of instrumental origin between hydroxylated silicates and organics, with organics usually having much more fractionated compositions, i.e. much lower D/H ratios, hence δD values, (Lévy et al. 2019). A transitional region of width about 1 to 1.5 µm corresponding to the primary ion beam overlapping on both Pt and phlogopite is visible on both elemental and

isotopic images. This demonstrates the feasibility of imaging variations of D/H ratios on the order of 100-200‰ at the 1-µm scale using this technique (Lévy et al. 2019). Fig. 10c shows the zone analyzed by NanoSIMS on the FIB section. After NanoSIMS analysis, the section was recovered and thinned down to ~1 µm for FTIR imaging using the synchrotron source. The corresponding spectrum obtained on the bulk FIB section is shown in Fig. 10d and is a typical phlogopite spectrum. An OH band is observed around 3650 cm^{-1} and a band corresponding to Si-O vibration is visible at ~1000 cm^{-1}. After FTIR analysis, the section has been thinned a second time down to a thickness of ~100 nm for TEM imaging and analysis (Fig. 10e). The acquired diffraction pattern and EDS analysis correspond to the CRPG phlogopite (Fig. 10f).

4. Application to the NWA 5515 chondrite

Individual sample preparation and analysis steps of our sequence were validated on standard mineral samples. Here, we present an example of application of our new sequence of analysis on a 35×35×15 µm-sized grain from the NWA 5515 CK chondrite. The full analytical sequence is summarized in Fig. 11 and Fig. 12.

As a first step, a 3D IR micro-tomography of the grain was acquired using our set-up. To improve the shape model and the quality of the IR 3D-reconstruction, X-ray micro-tomography was also performed on the grain (Fig. 11a-e). An average IR spectrum of the whole grain before and after X-ray micro-tomography was acquired and shows that X-ray tomography performed in our conditions (see paragraph 3.1.2) induced very little modifications of the extraterrestrial grain (Supplementary Figure 3). Two types of silicates were identified in the average spectrum of the whole sample: olivine with its spectral features at 908 and 964 cm^{-1} (Hamilton, 2010) and a Ca-poor pyroxene with a band at 1118 cm^{-1} (Beck et al., 2014). Fig. 11b-e show 3D-IR data superimposed onto X-ray data with IR reconstruction of silicates, organic matter and water. The 3D distributions of the two types of silicates were reconstructed using the area of one of the olivine band around 968 cm^{-1} (930-996 cm^{-1}) (Fig 11b) and the area of the orthopyroxene band around 1118 cm^{-1} (Fig 11c) (1094-1139 cm^{-1}). The organic matter and water 3D distributions were reconstructed using the CH bending vibration (1335-1425 cm^{-1}) (Fig 11d) and the OH bending vibration Fig (11e) (1570-1657 cm^{-1}) respectively. The 3D IR micro-tomography distribution of those phases shows that 1/ the silicates are distributed heterogeneously with the pyroxene phase near the tungsten needle, 2/ organic matter and water are also distributed heterogeneously but their distribution seems to be correlated. The grain thus shows three parts: a first region with only olivine without any hydratation signature or organic matter, a second region with olivine

showing alteration signatures with presence of organic matter and water and finally a last region with a pyroxene associated with organic matter and water.

After 3D analysis, the grain was recovered and cut in 5 slices, one of them was thinned down to 100nm for TEM analysis and the four others were thinned down to 2-3 microns for other 2D analysis (Supplementary Figure 4). 2D-IR and Raman maps as well as SEM images of slice 1 are shown in Fig. 12. 2D-IR maps and SEM images of slices 2 and 4 are shown in Supplementary Figure 5 and 6, respectively. 2D-IR maps, SE image and TEM images of slice 3 are shown in Supplementary Figure 7. As expected by the first analysis in 3D, 2D-maps of slice 1 reveal the presence of several types of silicates as well as organic matter and water that are distributed heterogeneously (Fig. 12f-j). Thanks to the better spectral resolution of the 2D IR spectra (4 cm^{-1}) than that of the 3D IR spectra (16 cm^{-1}), we were able to distinguish three types of silicates: olivine, a small pyroxene characterized by its 1118 cm^{-1} feature, and partially amorphous silicate that shows a weak pyroxene feature at 1118 cm^{-1} as well as a more large Si-O band between 880 and 1130 cm^{-1}. To better represent their 2D distribution, we mapped the area of one of the olivine band around 968 cm^{-1} (947-982), the minimum of the second derivative of the spectrum around 1118 cm-1 (Dionnet et al, 2018, 2020, Susi and Byler, 1983) and the peak position of the maximum between 868 and 930 cm^{-1}, for the olivine (Fig 12h), pyroxene (Fig 12f) and the partially amorphous pyroxene (Fig 12g), respectively. The grain consists predominantly of olivine, except the lower left corner, which consists of both crystalline and partially amorphous pyroxene. Organic matter and water distribution were also mapped using the area of the aliphatic CH bending modes between 1335 and 1425 cm^{-1} (Fig. 12i) and of the area of the OH bending mode between 1570 to 1657 cm^{-1} (Fig. 12j). They show a similar distribution with a concentration of organic matter and hydrated material in the left part of the grain enriched in pyroxene. The Raman map of band positions of mineral matter between 500 to 1000 cm^{-1} (Fig. 12d) confirms the presence of olivine (Fo70) with a doublet at 820 and 849 cm^{-1} and of a Ca-poor pyroxene (band at 945 cm^{-1}) (Huang et al, 2000). It also shows the presence of a magnetite grain (main band around 669 cm^{-1}). Finally, the Raman map of the intensity of the G band located around 1540 cm^{-1} (Fig. 12e) confirms the non-uniform distribution of the organic matter in slice 1. Composite X-ray map of Si, Mg, Fe, S, Ca (Fig 12 b) and EDS analyses confirms the presence of olivine (Fo65 to 70), low Ca-pyroxene (En60), two iron-oxide grains, a small ~2 µm FeNi-sulfide and two sub-micron-sized carbonate grains. SE and optical images (Fig 12a, c) show a good correlation between the mineralogical distribution and the morphological aspect of slice 1, notably with more visible cracks in the left part of the grain.

For slices 2,3,4, we also observe a good agreement of the silicates and organic distribution between 3D IR micro-tomography and 2D imaging (Supplementary Figures 5, 6 and 7). Slice 4 shows only olivine without organic matter or water (Supplementary Figure 5) whereas slice 2 shows the three types of silicates, as well as correlated organic matter and hydrated matter towards the pyroxene-rich part of the grain (Supplementary Figure 6). Slice 3 consists mainly of olivine. TEM images and 2D-IR maps show that a portion of olivine contains cracks filled with fragile material associated with OH signal (Supplementary figure 7).

The association of water, organics and cracks with partially amorphous pyroxene indicates that the pyroxene in the lower left part of the grain has suffered some degree of aqueous alteration (Brearley, 2006). By contrast, a large part of the grain consists of unaltered olivine. In detail, minor organics and water were also detected in the portion of olivine in contact with pyroxene, indicative of the aqueous alteration inside the grain. Insight on the origin of the aqueous alteration can be gained from the nature of the organics. The position of G band is relatively different from a classical extraterrestrial organic matter which points to terrestrial alteration, in agreement with the mild-weathering stage of NWA 5515 chondrite (Weisberg et al., 2009).

Taken together, these 2D and 3D results allow determination of the mineralogy, state of alteration, and association with organic matter at the 2 microns scale of a 35*35*50 µm-sized grain. As a complement of 3D IR and X-ray analyses, 2D analyses are mandatory because 1/ they provide a better lateral and spectral resolution and 2/ are necessary to correctly characterize the grain. For example, whereas the mid-IR technique cannot detect the presence of Fe-Ni sulfide contrary to SEM, using only SEM would not allow detection of water in the pyroxene or to distinguish pyroxene from partially amorphous pyroxene.

In a reverse approach, the 3D IR distribution could be used to locate precisely the regions of interest to slice the grain for 2D analysis, provided it is possible to demonstrate a good correlation between the 2D reconstructed slice extracted from the 3D reconstruction of the grain and the 2D-IR hyper-spectral map. The 2D-IR map of slice 1 was thus compared with the 2D reconstructed slice extracted from the 3D reconstruction of the grain at the approximate position of slice 1 (Fig11 f) (see Dionnet et al., 2020 for details). There is a very good agreement between the 2D IR reconstructed map and the real 2D IR map as shown by the comparison of Fig 11g-j and 12f-j. The phases present in the slice (olivine, pyroxene s.l., organic matter and water) are detected in similar locations in the two maps. This demonstrates that from the 3D IR images of our grain, we can decide the best location and

orientation to slice the grain by FIB in order to optimize the study of interesting spots/phases either in 2D IR or Raman or with the TEM (with a better spatial and spectral resolution).

5. Discussion and conclusions

We have developed new sample preparation and analytical procedures to extract a maximum of sub-micrometer structural, mineralogical, chemical, molecular and isotopic information from micrometric heterogeneous samples. The full analytical procedure is summarized in Fig. 13.

In this analytical sequence (Fig 13), a single µm-sized grain welded at the end of a holder needle can be imaged with several 3D analytical techniques such as IR or X-ray micro-tomography (Tsuchiyama et al., 2009, 2011, 2013, 2014, Yesiltas et al. 2014, Dionnet et al, 2020). IR micro-tomography is performed first, as it is a completely non-destructive technique, differently from XCT (Sears et al., 2016). Other 3D complementary analyses can also be performed such as X-ray fluorescence spectrometry, Raman, or X-ray micro-diffraction (e.g. Medjoubi et al., 2013, Somogyi et al., 2015, Yesiltas et al., 2018). From this dataset, it is possible 1/ to get a first quick look at the spatial distribution and abundance at the µm-scale of the anhydrous and hydrated mineral phases as well as of the carbonaceous matter, 2/ correlate this phase distribution with the 3D structure of the grain. Using these 3D data, selected sites could then be chosen and sliced using the FIB to be further explored at a nanometer scale in 2D.

One of the strengths of our approach is the possibility to combine many different 2D analytical techniques in almost any possible order according to the requirements of the study. Depending on the chosen combination of techniques, FIB sections of different thicknesses can be prepared for the analysis by 2D IR and Raman micro-spectroscopy (Dionnet et al., 2018), NanoSIMS isotopic or trace element mapping, TEM and nearly any sub-micron mapping techniques that can handle 100 nm to few microns-thick FIB sections (e.g., STXM, Le Guillou et al., 2013 or EBSD, Kodama et al., 2020). Such combination of sub-micrometer analytical methods could bring a wealth of combined information including isotopic composition of different minerals, phase relationships, phase abundances, crystallographic structures, distribution of molecular bonds such as OH or CH. Notably, as 1/ we have shown that during our sample preparation, organic matter that is mixed with mineral matter is preserved and little contaminated, and 2/ as we use different techniques to look at both minerals and organics, it is thus possible to observe spatial relationships between organic and mineral matter. Performing NanoSIMS analysis of H isotopes in organic materials before TEM observations also allows to avoid isotopic fractionation induced by

electron bombardment (De Gregorio et al. 2010, Laurent et al. 2015, Uesugi et al. 2019). Finally, with this sample preparation protocol it is possible to correlate not only several 3D analyses or different 2D characterization but also to place the 2D nanoscale analyses in the larger framework of the 3D microstructure (porosity, cracks, voids) and the 3D assembly of compositional units. This sample preparation protocol can also be applied to biological sample as demonstrated by a companion study on foraminifera (Aléon et al., in prep) focused on the correlative imaging of trace elements by NanoSIMS and nanostructure by TEM.

Overall, the loss of matter along the whole sequence is very small compared to the large amount of information obtained from a very small volume of matter, as small as 10*10*10 µm and compared to classical sample preparation techniques. Grains larger than 100 micrometer must be handled differently at the beginning of the analytical sequence. Especially, high-resolution 3D techniques are not always possible but after FIB section extraction, analysis may proceed similarly to the protocol described here (Fig. 13).

These analytical developments open thus new perspectives in the multi-technique analysis of small and rare organic/mineral samples. This procedure could be used to analyze precious meteoritic samples such as small desert meteorites (e.g. Newton et al., 1995, Floss et al., 2014), fossil meteorites (e.g. Schmitz et al. 2015), interplanetary dust particles or micrometeorites (e.g. Brunetto et al. 2011, Dobrica et al. 2012 or Nakamura et al., 2005) as well as precious extraterrestrial samples returned by on-going or future space missions such as Hayabusa2 or OSIRIS-REx (Watanabe et al., 2017, 2019, Jaumann et al. 2019, Hamilton et al., 2019, Lauretta et al., 2019). For example, from a single 10 µm CM chondrite-like grain, it is possible to determine the macro-, micro- and nano-structure, the distribution of -OH and -CH functions, the degree of hydration of minerals associated to the organics, the detection of localized isotopic anomalies or the isotopic composition of specific regions of interest. Using a similar approach, Matsumoto et al. (2019) evidence fossil asteroidal ice in the primitive meteorite Acfer 094. Using IR tomography and 2D mapping, as well as TEM and microspectroscopies after NanoSIMS analysis, our protocol is complementary of previously developed analytical coupling strategies.

In the case of the Hayabusa2 mission, this top-down sequence could also allow production of spectroscopic data in support of remote sensing astronomical observations and bridge remote sensing and in situ observations of Ryugu at macroscopic scale with the chemical and physical processes operating at the nanoscale. The sequence presented here could be completed for instance by 3D reflection IR spectroscopy for an accurate comparison with asteroidal surfaces, which is currently under development in our group

(Brunetto et al. 2020).

Acknowledgments

We thank Etienne Deloule for providing Bamble amphibole and CRPG phlogopite. We also thank Brigitte Zanda, the Museum National d'Histoire Naturelle for providing fragments of the Paris meteorite. We thank Guy Consolmagno for providing NWA 5515 meteorite fragments from the Vatican meteorite collection. We also warmly thank Christophe Sandt, Obadias Mivumbi, Paul Haghi-Ashtiani, Zahia Djouadi, Cateline Lanz and Donia Baklouti for help, advices, samples and discussions. We greatly thank the reviewers, Motoo Ito and an anonymous reviewer, and the associate editor Mike Zolensky for the constructive comments. This work was partly supported by the French RENATECH network, grants from Ile de France (DIM-ACAV) and SOLEIL (IR microscopic analyses) and grants from Labex CHARMMMAT, LaSIPS and Region Ile de France (TEM). It was also supported by the CNRS INSU PNP National Planetary Programm and by the Centre National d'Etudes Spatiales (CNES-France, Hayabusa2 mission).

References

Aléon-Toppani A., Brunetto R., Aléon J., Dionnet Z., Rubino S., Levy D., Troadec D., Borondics F., Brisset F. 2020. A Preparation Sequence for Multi-Analysis of Micrometer-Sized Extraterrestrial Samples. (abstract #2682). 51st Lunar and Planetary Science Conference. CD-ROM.

d'Hendecourt L., Rotundi A., Dumas P., Djouadi Z., Jamme F. 2011. Mid-IR, Far-IR, Raman micro-spectroscopy, and FESEM–EDX study of IDP L2021C5: Clues to its origin. *Icarus* 212: 896-910.

Bassim N.D., De Gregorio B.T., Kilcoyne A.L.D., Scott K., Chou T., Wirick S., Cody G. and Stroud R.M. 2012 Minimizing damage during FIB sample preparation of softmaterials. *Journal of Microscopy* 245: 288–301

Beck P., Garenne A., Quirico E., Bonal L., Montes-Hernandez G., Moynier F., and Schmitt B. 2014. Transmission infrared spectra (2–25 lm) of carbonaceous chondrites (CI, CM, CV–CK, CR, C2 ungrouped : Mineralogy, water, and asteroidal processes. *Icarus* 229:263–277.

Berger E.L. and Keller L.P. 2015 A Hybrid Ultramicrotomy-FIB Technique for Preparing Serial Electron Transparent Thin Sections from Particulate Samples. *Microscopy Today*

23: 18.

Brearley A. J. 2006. The action of water. In Meteorites and the early solar system II, edited by Lauretta D. S. and McSween H. Y. Tucson, Arizona: The University of Arizona Press. pp. 567–586.

Brunetto R., Aléon-Toppani A., Rubino S., Baklouti D., Borondics F., Dionnet Z., Djouadi Z., Lantz C., Nakamura T., Takahashi M., Troadec D., Tsuchiyama A. 2020. IR Micro-Spectroscopy and Micro-Tomography of Isolated Murchison Grains in Preparation of the Hayabusa2 Sample Return (abstract #1135). 2020. 51st Lunar and Planetary Science Conference. CD-ROM.

Cliff G. and Lorimer G.W. 1975. The quantitative analysis of thin specimens. *Journal of Microscopy* 103: 203-207.

De Gregorio, B. T., Stroud, R. M., Nittler, L. R., Alexander, C. M. O. 'D., Kilcoyne, A. L. D., Zega, T. J. 2010. Isotopic anomalies in organic nanoglobules from Comet 81P/Wild 2: Comparison to Murchison nanoglobules and isotopic anomalies induced in terrestrial organics by electron irradiation. *Geochimica et Cosmochimica Acta* 74: 4454-4470.

De Gregorio B. T., Stroud R. M., Cody G. D., Nittler L. R., Kilcoyne A. L. D., and Wirick S. 2011. Correlated microanalysis of cometary organic grains returned by Stardust. *Meteoritics & Planetary Science* 46: 1376-1396.

Dionnet Z., Aleon‐Toppani A., Baklouti D., Borondics F., Brisset F., Djouadi Z., Sandt C., Brunetto R. 2018. Organic and mineralogic heterogeneity of the Paris meteorite followed by FTIR hyperspectral imaging. *Meteoritics & Planetary Science* 53: 2608-2623.

Dionnet Z., Brunetto R., Aléon-Toppani A., Baklouti D., Borondics F., Buellet A-C., Djouadi, Z., Nakamura T., Rubino S., Sandt C. and Tsuchiyama A. 2020. Combining IR and X-ray micro-tomography datasets: Application to Itokawa particles and to Paris meteorite. *Meteoritics & Planetary Science* 55: 1645-1664.

Dobrică E., Engrand C., Leroux H., Rouzaud J. -N., Duprat J. 2012. Transmission Electron Microscopy of CONCORDIA UltraCarbonaceous Antarctic MicroMeteorites (UCAMMs): Mineralogical properties. *Geochimica et Cosmochimica Acta* 76: 68-82

Eswara S., Pshenova A., Yedra L., Hoang Q. H., Lovric J., Philipp P., and Wirtz T. 2019. Correlative microscopy combining transmission electron microscopy and secondary ion mass spectrometry: A general review on the state-of-the-art, recent developments, and prospects. *Appl. Phys. Rev.* 6: 021312.

Floss C., Le Guillou C., Brearley A. 2014. Coordinated NanoSIMS and FIB-TEM analyses of organic matter and associated matrix materials in CR3 chondrites. *Geochimica et Cosmochimica Acta* 139: 1–25.

Giannuzzi L. A. and Stevie F. A. 1999. A review of focused ion beam milling techniques for TEM speciment preparation. *Micron* 30: 197-204.

Govindaraju K. 1994. Compilation of working values and sample description for 383 geostandards. *Geostandards Newsletter* 18: 1-158.

Hamilton V. E., Simon A. A., Christensen P.R., Reuter D. C., Clark B. E., Barucci M. A., Bowles N. E., Boynton W. V., Brucato J. R., Cloutis E. A., Connolly Jr. H. C.,. Donaldson Hanna K. L, Emery J. P., Enos H. L., Fornasier S., Haberle C. W., Hanna R. D., Howell E. S., Kaplan H. H., Keller L. P., Lantz C., Li J.-Y., Lim L. F., McCoy T. J., Merlin F., Nolan M. C., Praet A., Rozitis B., Sandford S. A., Schrader D. L., Thomas C. A., Zou X.-D., Lauretta D. S. and the OSIRIS-REx Team. 2019. Evidence for widespread hydrated minerals on asteroid (101955) Bennu. *Nature Astronomy* 332: 332–340.

Hamilton V.E. 2010. Thermal infrared (vibrational) spectroscopy of Mg–Fe olivines : A review and applications to determining the composition of planetary surfaces. *Chemie der Erde - Geochemistry* 70: 7-33.

Heaney P. J., Vicenzi E. P., Giannuzzi L. A. and Livi K. J. T. 2001. Focused ion beam milling: A method of site-specific sample extraction for microanalysis of Earth and planetary materials. *American Mineralogist* 86: 1094-1099.

Hewins R., Bourot-Denise M., Zanda B., Leroux H., Barrat J.A., Humayun M., Gopel C., Greenwood R.C., Franchi I.A., Pont S., Lorand J.P., Cournède C., Gattacceca J., Rochette P., Kuga M., Marrocchi Y., Marty B. 2014 The Paris meteorite, the least altered CM chondrite so far. *Geochimica et Cosmochimica Acta* 124: 190–222.

Huang E., Chen C.H., Huang T., Lin E.H. and Xu J.A. 2000 Raman Spectroscopic characteristics og Mg-Fe-Ca pyroxenes. *American mineralogist* 85: 473-479.

Ito M., Tomioka N., Uesugi K., Uesugi M., Kodama Y., Sakurai I., Okada I., Ohigashi T., Yuzawa H., Yamaguchi A., Imae N., Karouji Y., Shirai N., Yada T.and Abe M. 2020 The universal sample holders of microanalytical instruments of FIB, TEM, NanoSIMS, and STXM−NEXAFS for the coordinated analysis of extraterrestrial materials. *Earth, Planets and Space* 72: 133

Jaumann R., Schmitz, N., Ho, T. -M., Schröder, S. E., Otto, K. A., Stephan, K., Elgner, S., Krohn, K., Preusker, F., Scholten, F., Biele, J., Ulamec, S., Krause, C., Sugita, S., Matz, K. -D., Roatsch, T., Parekh, R., Mottola, S., Grott, M., Michel, P. Trauthan, F., Koncz, A., Michaelis, H., Lange, C., Grundmann, J. T., Maibaum, M., Sasaki, K., Wolff, F., Reill, J., Moussi-Soffys, A., Lorda, L., Neumann, W., Vincent, J. -B., Wagner, R., Bibring, J. -P., Kameda, S., Yano, H., Watanabe, S., Yoshikawa, M., Tsuda, Y. , Okada, T., Yoshimitsu, T., Mimasu, Y., Saiki, T., Yabuta, H., Rauer, H., Honda, R., Morota, T., Yokota, Y., Kouyama, T. 2020 Images from the surface of asteroid Ryugu show rocks similar to carbonaceous chondrite meteorites. 2019. *Science* 365: 817-820.

Kleindiek S., Rummel A., Schock K. 2008. E-beam hardening SEM glue for fixation of small objects in the SEM. In: Luysberg M., Tillmann K., Weirich T. EMC 2008 14th European Microscopy Congress, Aachen, Germany. Springer, Berlin, Heidelberg. https://doi.org/10.1007/978-3-540-85156-1_283.

Kodama Y., Tomioka N., Ito M. and Imae N. 2020. Developments in microfabrication of mineral samples for simultaneous EBSD–EDS analysis utilizing an FIB–SEM instrument: study on an S–type cosmic spherule from Antarctica. *Journal of Mineralogical and Petrological Sciences* 115: 407–415.

Laurent, B., Roskosz, M., Remusat, L., Robert, F., Leroux, H., Vezin, H., Depecker, C., Nuns, N., Lefebvre, J.-M. 2015. The deuterium/hydrogen distribution in chondritic organic matter attests to early ionizing irradiation. *Nature Communications* 6: 8567.

Lauretta D., DellaGiustina D., Bennett C., Golish D., Becker K., Balram-Knutson S., Barnouin O., Becker T., Bottke W., Boynton W., Campins H., Clark B., Connolly Jr H., Drouet d'Aubigny C., Dworkin J., Emery J., Enos H., Hamilton V., Hergenrother C., Howell E., Izawa M., Kaplan H., Nolan M., Rizk B., Roper H., Scheeres D., Smith P., Walsh K., Wolner C. and The OSIRIS-REx Team. 2019. The unexpected surface of asteroid (101955) Bennu. *Nature* 568: 55–60.

Le Guillou C., Remusat L., Bernard S., Brearley A. J., Leroux H. 2013. Amorphization and D/H fractionation of kerogens during experimental electron irradiation: Comparison with chondritic organic matter. *Icarus* 226: 101–110.

Lee M., Bland P and Graham G. 2003. Preparation of TEM samples by focused ion beam (FIB) techniques: applications to the study of clays and phyllosilicates in meteorites. *Mineralogical Magazine* 67:581-592.

Lévy D., Aléon J., Aléon-Toppani A., Troadec D., Duhamel R., Gonzalez-Cano A., Bureau H., and Khodja H. 2019. NanoSIMS Imaging of D/H Ratios on FIB Sections. *Anal. Chem.* 91: 13763−13771.

Martina P.G., Griffithsb I., Jonesa C.P., Stitta C.A., Davies-Milnerc M., Mosselmansd J.F.W., Yamashikie Y., Richardsf D.A., Scotta T.B. 2016. In-situ removal and characterisation of uranium-containing particles from sediments surrounding the Fukushima Daiichi Nuclear Power Plant. *Spectrochimica Acta Part B* 117: 1–7.

Matrajt G., Ito M., Wirick S., Messenger S., Brownlee D. E., Joswiak D., Flynn G., Sandford S., Snead C., and Westphal A. 2008. Carbon investigation of two Stardust particles: A TEM, NanoSIMS, and XANES study. *Meteoritics & Planetary Science* 43: 315–334.

Matsumoto M., Tsuchiyama A., Nakato A., Matsuno J., Miyake A., Kataoka A., Ito M., Tomioka N., Kodama Y., Uesugi K., Takeuchi A., Nakano T., Vaccaro E. 2019. Discovery of fossil asteroidal ice in primitive meteorite Acfer 094. *Sci. Adv.* 5: eaax5078.

Mayer J., Giannuzzi L. A., Kamino T. and Michael J. 2007. TEM Sample Preparation and FIB-Induced Damage. *MRS Bulletin* 32: 400–407.

Medjoubi K., Leclercq N., Langlois F., Buteau A., Lé S., Poirier S., Mercère P., Sforna M-C., Kewish C.M., Somogyi A. 2013. Development of fast, simultaneous and multi‑technique scanning hard X‑ray microscopy at Synchrotron Soleil. *Journal of synchroton radiation* 20: 293-299.

Messenger S., Keller L. P., Lauretta D. S. 2005. Supernova Olivine from Cometary Dust. *Science* 309: 737-741.

Nakamura T., Noguchi T., Ozono Y., Osawa T., and Nagao K. 2005. Mineralogy of ultracarbonaceous large micrometeorites. *Meteoritics & Planetary Science* 40 (Suppl): 5046.pdf.

Nakamura T., Noguchi T., Tanaka M., Zolensky M.E., Kimura M., Tsuchiyama A., Nakato A., Ogami T., Ishida H., Uesugi M., Yada T., Shirai K., Fujimura A., Okazaki R., Sandford S.A., Ishibashi Y., Abe M., Okada T., Ueno M., Mukai T., Yoshikawa M., Kawaguchi J. 2011. Itokawa dust particles: a direct link between S-type asteroids and ordinary chondrites. *Science* 333: 1113–1116.

Newton J., Bischoff A., Arden J. W., Franchi I. A., Geiger T., Greshake A., Pillinger C. T. 1995. Acfer 094, a uniquely primitive carbonaceous chondrite from the Sahara. *Meteoritics & Planetary Science* 30: 47-56.

Nguyen, A. N., Stadermann F. J., Zinner E., Stroud R. M., Alexander C. M. O. and Nittler L. R. 2007. Characterization of Presolar Silicate and Oxide Grains in Primitive Carbonaceous Chondrites. *Astrophysical Journal* 656: 1223-1240.

Noun M., Baklouti D., Brunetto R., Borondics F., Calligaro T., Dionnet Z., d'Hendecourt L., et al. 2019. A Mineralogical Context for the Organic Matter in the Paris Meteorite Determined by A Multi-Technique Analysis. *Life* 9, 44.

Penen F., Malherbe J., Isaure M.-P., Dobritzsc D., Bertalan,I., Gontier, E., Le Coustumer, P., Schaumlöffel, D. J. 2016. Chemical bioimaging for the subcellular localization of trace elements by high contrast TEM, TEM/X-EDS, and NanoSIMS. *J. Trace Elem. Med. Biol.* 37: 62-68.

Sandt, C., Dionnet, Z., Toplak, T., Fernandez, E., Brunetto, R., Borondics, F. (2019) Performance comparison of aperture-less and confocal infrared microscopes. Journal of Spectral Imaging 8: a8.

Sears D., Sears H., Ebel D., Wallace S., and Friedrich J. 2016. X-ray computed tomography imaging: A not-so-nondestructive technique. *Meteoritics & Planetary Science* 51: 833–838.

Shirai N., Karouji Y., Kumagai K., Uesugi M., Hirahara K., Ito M., Tomioka N., Uesugi K., Yamaguchi A., Imae N., Ohigashi T., Yada T. and Abe M. 2020. The effects of possible contamination by sample holders on samples to be returned by Hayabusa2. *Meteoritics & Planetary Science* 55: 1665–1680.

Simon S., Joswiak D., Ishii H., Bradley J., Chi M., Grossman L., Aléon J., Brownlee D., Fallon S., Hutcheon I., Matrajt G., and McKeegan K. 2008. A refractory inclusion returned by Stardust from comet 81P/Wild 2. *Meteoritics & Planetary Science* 43: 1861–1877.

Smith J., Dai Z., Weber P., Graham G., Hutcheon I., Bajt S., Ishii H., Bradley J. 2005. Nitrogen isotopic anomalies in a hydrous interplanetary dust particle. (abstract #1003). 36st Lunar and Planetary Science Conference.

Somogyi A., Medjoubi K., Baranton G., Le Roux V., Ribbens M., Polack F., Philippotb P. and Samamaa J.P. 2015. Optical design and multi-length-scale scanning spectro-microscopy possibilities at the Nanoscopium beamline of Synchrotron Soleil. *Journal of synchroton radiation* 22: 1118-1129.

Stadermann F. J., Croat T. K., Bernatowicz T. J., Amari S., Messenger S., Walker R. M. and Zinner E. 2005. Supernova graphite in the NanoSIMS: Carbon, oxygen and titanium

isotopic compositions of a spherule and its TiC sub-components. *Geochimica et Cosmochimica Acta*. 69: 177-188.

Suer T.-A., Siebert J., Remusat L., Menguy N., Fiquet G. 2017. A sulfur-poor terrestrial core inferred from metal–silicate partitioning experiments. *Earth and Planetary Science Letters* 469, 84–97.

Susi H. and Byler D. M. 1983. Protein structure by Fourier transform infrared spectroscopy: Second derivative spectra. *Biochemical and Biophysical Research Communications* 115:391–397.

Tsuchiyama A., Nakamura T., Okazaki T., Uesugi K., Nakano T., Sakamoto K., Akaki T., Iida Y., Kadono T., Jogo K., Suzuki Y. 2009. Three-dimensional structures and elemental distributions of Stardust impact tracks using synchrotron microtomography and X-ray fluorescence analysis. *Meteoritics & Planetary Science* 44, 1203-1224.

Tsuchiyama A., Uesugi M., Matsushima T., Michikami T.,Kadono T., Nakamura T., Uesugi K., Nakano T., Sandford S. a, Noguchi R., Matsumoto T., Matsuno J., Nagano T., Imai Y., Takeuchi A., Suzuki Y., Ogami T., Katagiri J., Ebihara M., Ireland T. r, Kitajima F., Nagao K., Naraoka H., Noguchi T., Okazaki R., Yurimoto H., Zolensky M. E., Mukai T., Abe M., Yada T., Fujimura A., Yoshikawa M., and Kawaguchi J. 2011. Three-Dimensional Structure of Hayabusa Samples: Origin and Evolution of Itokawa Regolith. *Science* 333: 1125-1128.

Tsuchiyama A., Nakano T., Uesugi K., Uesugi M., Takeuchi A., Suzuki Y., Noguchi R., Matsumoto T., Matsuno J., Nagano T., Imai Y., Nakamura T., Ogami T., Noguchi T., Abe M., Yada T., and Fujimura A. 2013. Analytical dual-energy microtomography: A new method for obtaining three-dimensional mineral phase images and its application to Hayabusa samples. *Geochimica et Cosmochimica Acta* 116: 5-16.

Tsuchiyama A., Uesugi M., Uesugi K., Nakano T., Noguchi R., Matsumoto T., Matsuno J., Nagano T., Imai Y., Shimada A., Takeuchi A., Suzuki Y., Nakamura T., Noguchi T., Abe M., Yada T., Fujimura A. 2014. Three-dimensional microstructure of samples recovered from asteroid 25143 Itokawa: Comparison with LL5 and LL6 chondrite particles. *Meteoritics & Planetary Science* 49, 172-187.

Uesugi M., Ito M., Yabuta H., Naraoka H., Kitajima F., Takano Y., Mita H., Kebukawa Y., Nakato A., Karouji Y. 2019 Further characterization of carbonaceous materials in Hayabusa‐returned samples to understand their origin. *Meteoritics and Planetary science* 54: 638-666.

Uesugi M., Hirahara K., Uesugi K., Takeuchi A., Karouji Y., Shirai N., Ito M., Tomioka N., Ohigashi T., Yamaguchi A., Imae N., Yada T., and Abe M. 2020 Development of a sample holder for synchrotron radiation-based computed tomography and diffraction analysis of extraterrestrial materials *Review of Scientific Instruments* 91, 035107.

Watanabe S., Hirabayashi M., Hirata N., Hirata N., Noguchi R., Shimaki Y., Ikeda H., Tatsumi E., Yoshikawa M.,Kikuchi S., Yabuta H., Nakamura T., Tachibana S., Ishihara Y., Morota T., Kitazato K., Sakatani N., Matsumoto K., Wada K., Senshu H., Honda C., Michikami T., Takeuchi H., Kouyama T., Honda R., Kameda S., Fuse T., Miyamoto H., Komatsu G., Sugita S., Okada T., Namiki N., Arakawa M., Ishiguro M., Abe M., Gaskell R., Palmer E., Barnouin O. S., Michel P., French A. s, McMahon J. W., Scheeres D. J., Abell P. A., Yamamoto Y., Tanaka S., Shirai K., Matsuoka M., Yamada M., Yokota Y., Suzuki H., Yoshioka K., Cho Y., Tanaka S., Nishikawa N., Sugiyama T., Kikuchi H., Hemmi R., Yamaguchi T., Ogawa N., Ono G., Mimasu Y., Yoshikawa K., Takahashi T., Takei Y., Fujii A., Hirose C., Iwata T., Hayakawa M., Hosoda S., Mori O., Sawada H., Shimada T., Soldini S., Yano H., Tsukizaki R., Ozaki M., Iijima Y., Ogawa K., Fujimoto M., Ho T-m, Moussi A., Jaumann R., Bibring J-P., Krause C., Terui F., Saiki T., Nakazawa S., and Tsuda Y. 2019. Hayabusa2 arrives at the carbonaceous asteroid 162173 Ryugu—A spinning top–shaped rubble pile. *Science* 364: 268-272.

Watanabe S., Tsuda Y., Yoshikawa M., Tanaka S., Saiki T. and Nakazawa S. 2017. Hayabusa2 Mission Overview. *Space Science Reviews* 208: 3-16

Weisberg M. K., Smith C., Benedix G., Herd C.D.K., Righter K., Haack H., Yamaguchi A., Chennaoui Aoudjehane H. and Grossman J.N. 2009. The Meteoritical Bulletin, No. 96, September. *Meteoritics & Planetary Science* 44: 1355–1397.

Yesiltas M., Jaret S., Young J., Wright S.P. and Glotch T.D. 2018. Three-Dimensional Raman Tomographic Microspectroscopy: A Novel Imaging Technique. *Earth and Space Science* 5: 380– 392.

Yesiltas M., Kebukawa, Y., Peale, R.E., Mattson E., Hirschmugl C.J. and Jenniskens P. 2014. Infrared imaging spectroscopy with micron resolution of Sutter's Mill meteorite grains. *Meteoritics & Planetary Science* 49: 2027-2037.

Zolensky M., Nakamura-Messenger K., Fletcher L., and See L. 2008. Curation, spacecraft recovery, and preliminary examination for the Stardust mission: A perspective from the curatorial facility. *Meteoritics & Planetary Science* 43: 5–21.

FIGURE CAPTIONS:

Fig. 1: Secondary electron images illustrating the welding of two grains from NWA5515 chondrite using Platinium (a-d) and electronic glue (e-h). (a,e) grains deposited on gold substrate. (d,h) lifting of the grain. (b) contact between the holder needle and the grain. (c) details of the welding between the needle and the grain. (f) tip of the needle with liquid e-glue. (g) contact between the needle and the grain after polymerization of the grain. Arrows in (c) and (g) indicate the contact between the grain and the needle.

Fig. 2: Raman analysis of the carbon contamination deposited during welding using Pt or electronic glue. (a) Raman spectra of the contamination related to the welding with Pt and e-glue compared with the Raman spectrum of the organic matter from the Paris meteorite. The Raman spectrum of the Paris meteorite shows classical D and G bands of poly-aromatic carbons, with the G band peaking around 1590-1600 cm^{-1}, whereas the carbon from the Pt-welding is amorphous and shows a large band around ~1500-1560 cm^{-1} with a shoulder around 1350 cm^{-1}. Finally, in this spectral range, the e-glue does not show any visible signature, but only a strong fluorescence signal. (b) Intensity (counts per second) versus G-band position (cm^{-1}) measured from the welding point towards a grain of the Paris meteorite. This graph shows (1) that the surface amorphous carbon contamination is restricted to the surroundings of the welding point (between 2.5 and 5 µm at most) and (2) its intensity is relatively weak.

Fig. 3: IR analysis of the carbon contamination deposited during welding using e-glue. (a) IR spectra extracted from the hyper-spectral mapping of a grain of the Paris meteorite: one is from the e-glue located at the tip of the holder needle and the other one is from a spot of the meteorite rich in organic matter (see location in b). (b) Secondary electron image (upper right), IR hyper-spectral mapping of the grain (upper left), and distinct distributions of the 1711 (lower left) and 1603 (lower right) cm^{-1} band in the grain and e-glue.

Fig. 4: (a) Secondary electron image of a calcite grain Pt-welded at the tip of a W needle and (b) IR micro-tomography reconstruction of the calcite grain. In red is shown the spatial distribution of the calcite based on its thin 2520 cm^{-1} band whereas in grey is shown the 3D reconstruction of the spectral continuum around 3500 cm^{-1}, which includes scattering, diffraction and absorption of both grain and needle. A filter was applied to the calcite distribution to remove scattering artifacts at the edges of the grains. Note that the orientation of the grain may be slightly different from that of the SE image.

Fig. 5: Secondary electron (a-f, i) and ion (g, h) images of the recovery and slicing of an olivine grain. (a) Deposition of the grain on a conductive substrate, (b) olivine grain free of the holder needle, the arrow indicates the remaining Pt welding that was cut in order to recover the grain, (c) deposition of a protective/cohesive layer of Pt over the whole grain, (d and e) cutting of the grain in 3 slices, (f) lifting of one slice with the needle from the micro-manipulator, (g) welding of the slice on a special TEM M-grid, (h) deposition of a thick slice on a Al-substrate. Note that the rectangular dotted-lines correspond to marks that were previously made on the wafer, (i) detail of one of the slices showing the grain rimmed by the Pt-layer.

Fig. 6: IR and Raman spectra of a ~700 nm thick slice extracted from a 10×20 µm grain of olivine. IR spectrum was acquired within the grain using an aperture of 8*8 micron and a resolution of 8 cm^{-1}. Typical peaks of olivine are observed on the spectra (~838 cm^{-1}, ~875 cm^{-1}, 980 cm^{-1}). Raman spectra of the sample were measured both in the grain and in the Pt-layer rimming the grain. Spectral resolution is 4 cm^{-1} and spatial resolution is around 1 µm. Typical Raman shift of San Carlos olivine are observed for the interior of the grain (822 cm^{-1} and 855/856 cm^{-1}). The Pt rim shows a large band with a peak centered on ~1530 cm^{-1} and a shoulder on ~1350 cm^{-1} corresponding to the G and D bands of amorphous carbon.

Fig. 7: Electron images of the preparation of the NanoSIMS section on Pt bridge (a-d) and recovery after NanoSIMS analysis for further analyses (e-h). (a) Extraction of a thick FIB section from a sample, (b) deposition of the slice on two Pt stripes, (c) welding of the section to the stripes (d) lifting of the needle after sectioning the needle from the slice, (e) FIB section after NanoSIMS analysis showing the analysis crater, (f) Total and partial sectioning of the border of the slice, (g) welding of the needle to one side of the section and final sectioning of the border of the slice, (h) lifting of the free slice.

Fig. 8: Hydrogen isotopic composition of Bamble amphibole analyzed with different sample preparations, uncorrected for instrumental mass fractionation. The similar values obtained for the polished section, the FIB section deposited on Al disk and the FIB section mounted on Pt bridge indicate absence of additional instrumental bias due to FIB section preparation and mounting within errors.

Fig. 9: Cartoon summarizing the cross-section of a FIB section prepared for combined NanoSIMS, FTIR and TEM analyses. The top part exposed to the first NanoSIMS analysis is shown to the right. Once the section is recovered from NanoSIMS analysis, the red 500 nm to 1 µm thick layer (1) has been consumed and the green <10 nm thick layer (2) damaged

by the ion beam is removed in the FIB-SEM. After FTIR the back part of the section (500 nm to 1 µm) (4) is removed in the FIB-SEM, leaving a thin (~ 100 nm thick) electron transparent section (3). Layers (5) are the borders of the FIB section, which are contaminated by Pt from the FIB welding. This procedure allows to analyze by FTIR and TEM a portion of the section immediately adjacent to the bottom of the material analyzed by NanoSIMS, i.e. corresponding to the end of the NanoSIMS analysis.

Figure 10: Complete analytical sequence of a 3 µm-thick FIB section from the CRPG phlogopite. (a) NanoSIMS ion image of hydrogen. The image overlaps on the phlogopite and the Pt strap, which has higher H^- intensities (given in counts/second) due to the presence of organometallic H (b) Corresponding NanoSIMS image of D/H ratio. (c) SE image of the FIB section after NanoSIMS. Notice the presence of a crater corresponding to the analysed zone and overlapping on phlogopite and the Pt strap (black dotted rectangle). The dark area corresponds to a larger area sputter-cleaned at the beginning of NanoSIMS analysis. d) Section recovered and thinned down to 1 micron for FTIR. e) Baseline corrected FTIR spectrum of the phlogopite spectrum. The optical image of the section in the IR microscope is shown in the corner. f) Diffraction pattern of phlohopite acquired on the section with the TEM after final thinning.

Figure 11: 3D reconstruction of a 35×35×15 µm-sized grain extracted from the NWA chondrite, and mounted on a tungsten needle. a) Secondary electron image of the grain (b-e) 3D-IR data superimposed onto X-ray data, with IR reconstruction of (b) olivine and (c) pyroxene s.l., (d) organic matter and (e) water. The 3D spatial distributions of the silicates were reconstructed using the area of one of the olivine band around 968 cm-1 (in the 930-996 cm^{-1} range) and the area of the Ca-poor pyroxene band around 1118 cm-1 (in the 1094-1139 cm^{-1} range). The organic matter and water were reconstructed using the area of the aliphatic (1335-1425 cm^{-1}) and of the OH (1570-1657 cm^{-1}) bending modes respectively. f/ sectional plan showing the location of the slice that is extracted from the 3D-IR reconstructed sample (see Dionnet et al., 2020 for details). (g-j) 2D slices virtually extracted from the 3D reconstruction of the NWA-5515 grain. IR bands are the same as those used to show the 3D spatial distribution of the silicates, the organic matter and water. (g) IR olivine band, (h) IR Ca-poor pyroxene 1118 cm^{-1} band, (i) IR CH band and (j) IR OH bending band. Note that, because of the diffraction limited spatial resolution, some artifacts are present at the edges of the 2D extracted slices.

Figure 12: Scanning electron microscopy, Raman and IR spectroscopy studies of the slice 1 that was extracted from the NWA5515 grain using FIB (note that the orientation of the slice

may slightly vary from one technique to the other, due to a tilt in some geometric configurations). (a) Backscattered electron image. (b) composite X-ray map of Si (Red), Mg (green), Fe (blue), S (Grey), Ca (Yellow) showing the presence of two iron oxides in dark blue, an iron sulfide in light blue, two very small carbonate grains in bright yellow, olivine in yellow and a more pyroxene-rich zone in red, (c) bright-field optical image, (d) Raman map of band positions of minerals between 500 to 1000 cm^{-1} Raman shift showing the presence of olivine (Fo70) in orange (doublet at 820 and 849 cm^{-1}), pyroxene in yellow (main band at 945 cm^{-1}) and magnetite in purple (main band around 669 cm^{-1}), (e) Raman map of the intensity of the G band located around 1540 cm^{-1}. The raman maps were acquired with a 1,5 µm spatial sampling. (f-j) 2D-IR hyper-spectral maps (spatial sampling of 0.66 µm) acquired using the FPA detector of (f) the minimum of the second derivative of the spectrum around 1118 cm^{-1} for pyroxene, (g) the main peak position between 868 and 930 cm^{-1} for partially amorphous pyroxene, (h) the area of olivine band around 968 cm^{-1} (947-982 cm^{-1} range), (i) the area of aliphatic CH bending modes between 1335 and 1425 cm^{-1}, (j) the area of OH bending mode between 1570 to 1657 cm^{-1}. Maps show the presence of olivine in a large part of the grain, in addition to pyroxene and partially amorphous pyroxene, whose presence correlates with that of organic matter and water.

Figure 13: Cartoon summarizing the new sample preparation and analytical procedures.

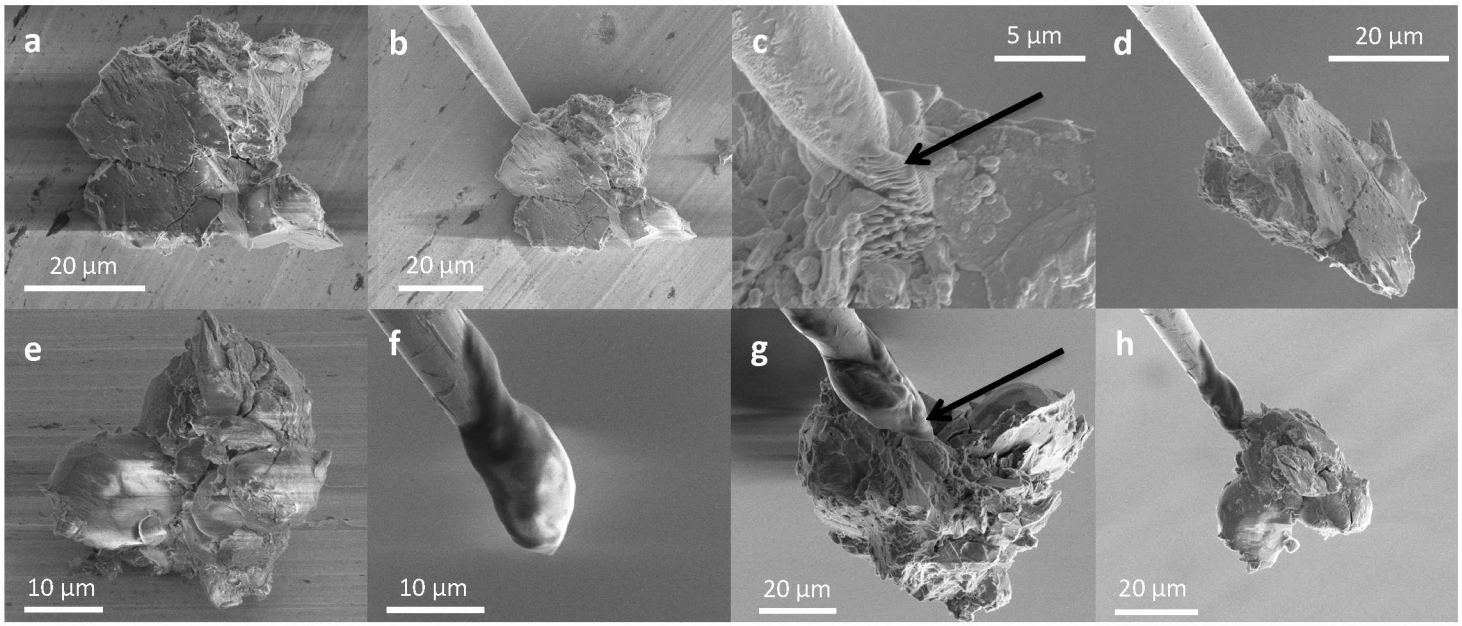

FIG 1

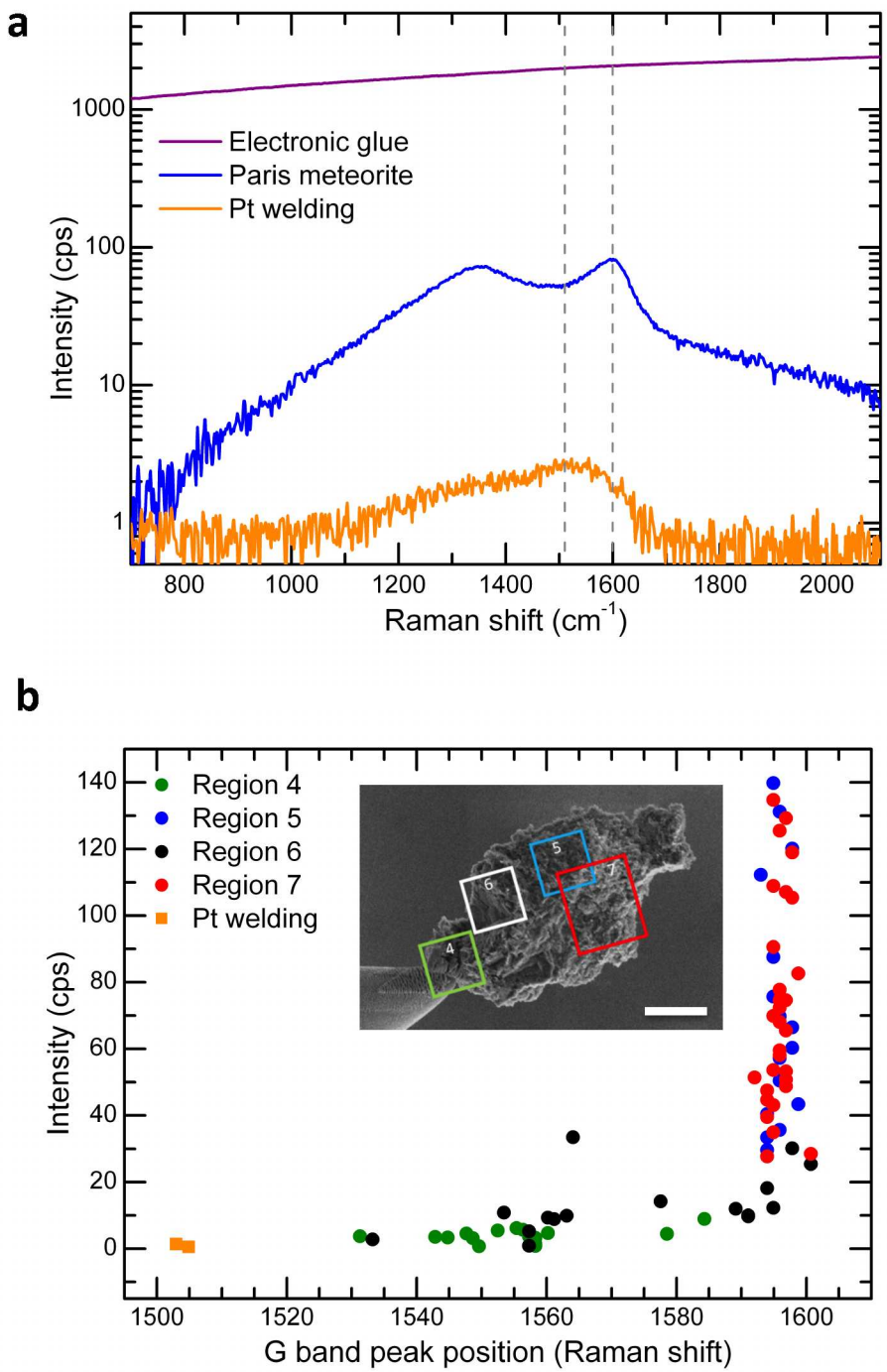
a
1000
100
10
1
Intensity (cps)
Electronic glue
Paris meteorite
Pt welding
800
1000
1200
1400
1600
1800
2000
Raman shift (cm-1)
b
140
120
100
80
60
40
20
0
Intensity (cps)
Region 4
Region 5
Region 6
Region 7
Pt welding
4
5
6
7
1500
1520
1540
1560
1580
1600
G band peak position (Raman shift)

FIG 2

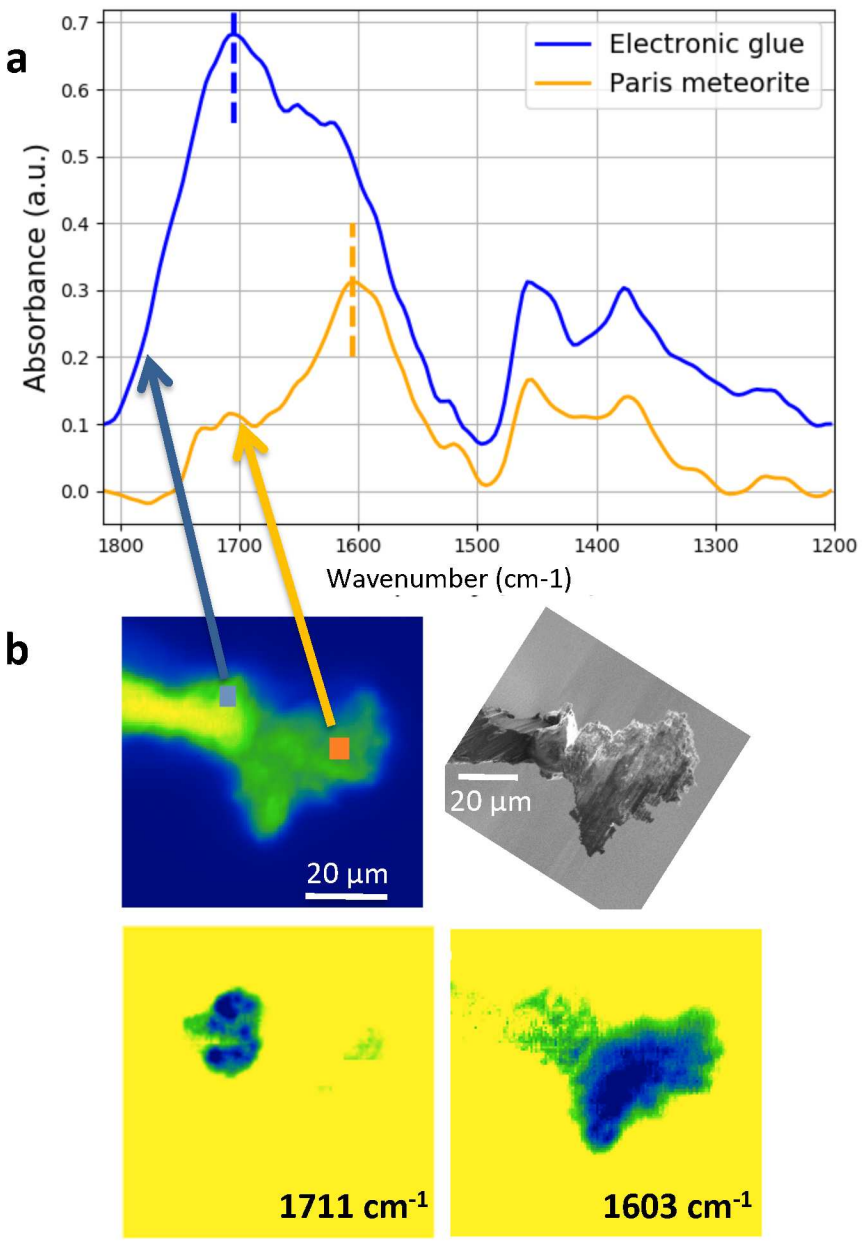
a
Electronic glue
Paris meteorite
Absorbance (a.u.)
0.7
0.6
0.5
0.4
0.3
0.2
0.1
0.0
1800
1700
1600
1500
1400
1300
1200
Wavenumber (cm-1)
b
20 µm
20 µm
1711 cm-1
1603 cm-1

FIG 3

Fig.4

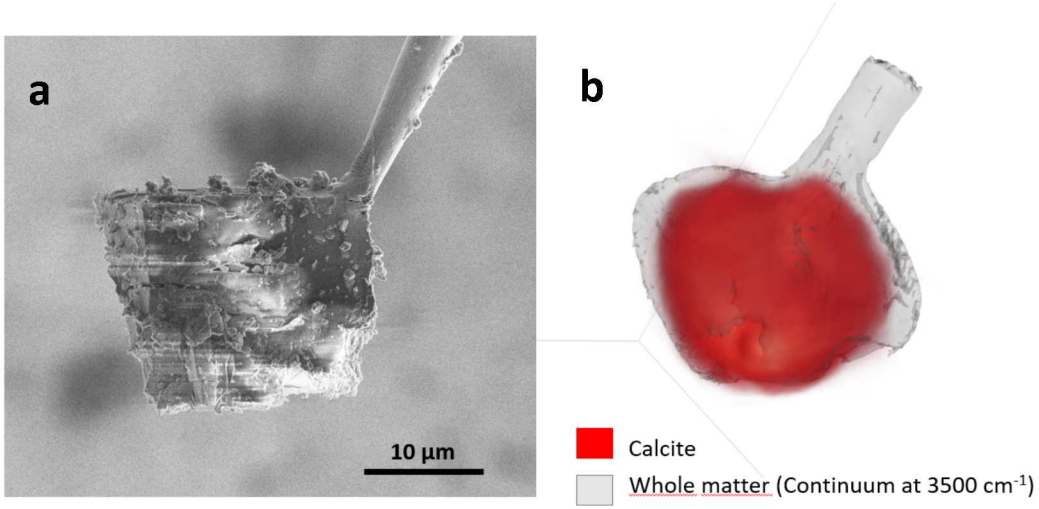

FIG 4

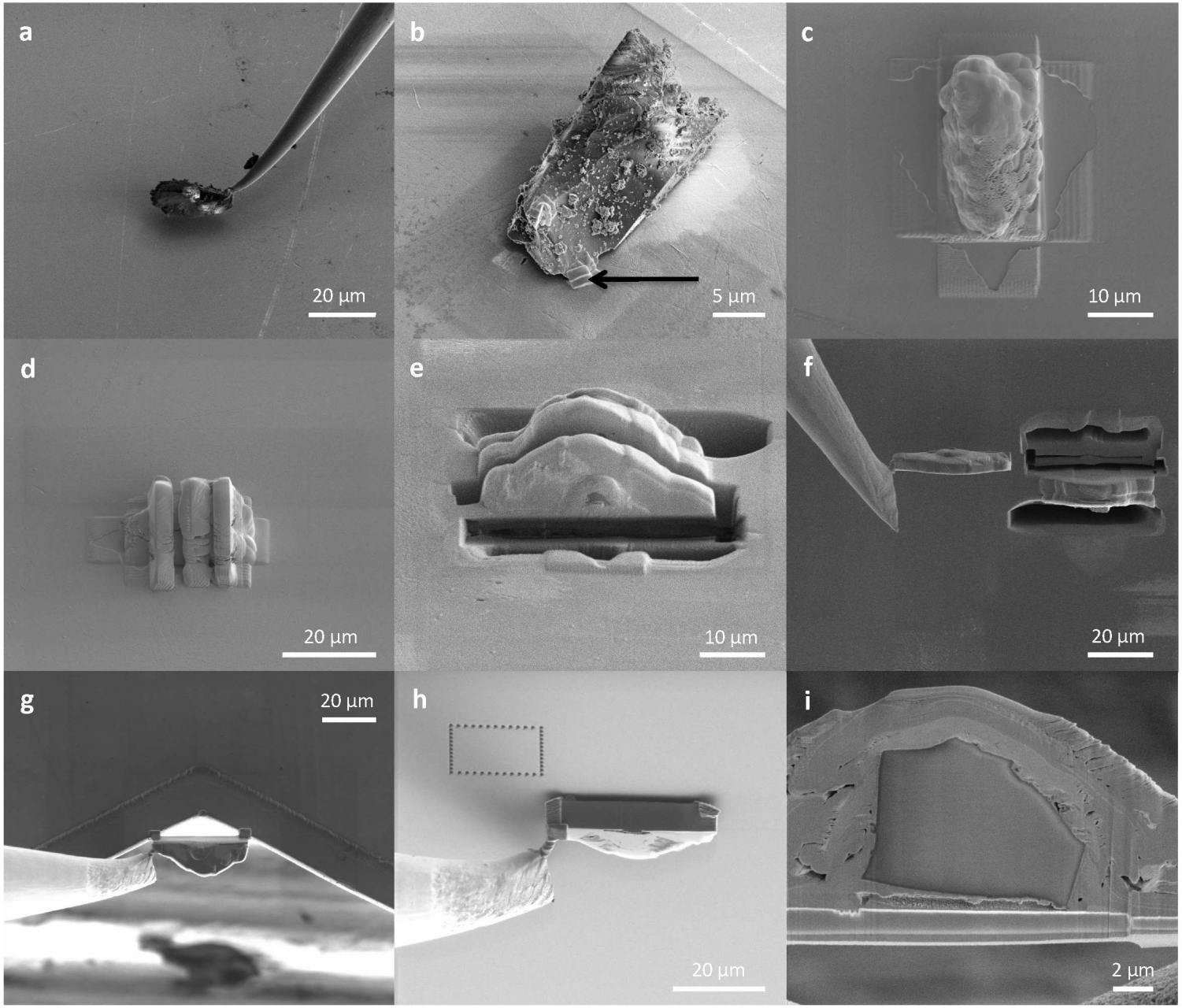

FIG 5

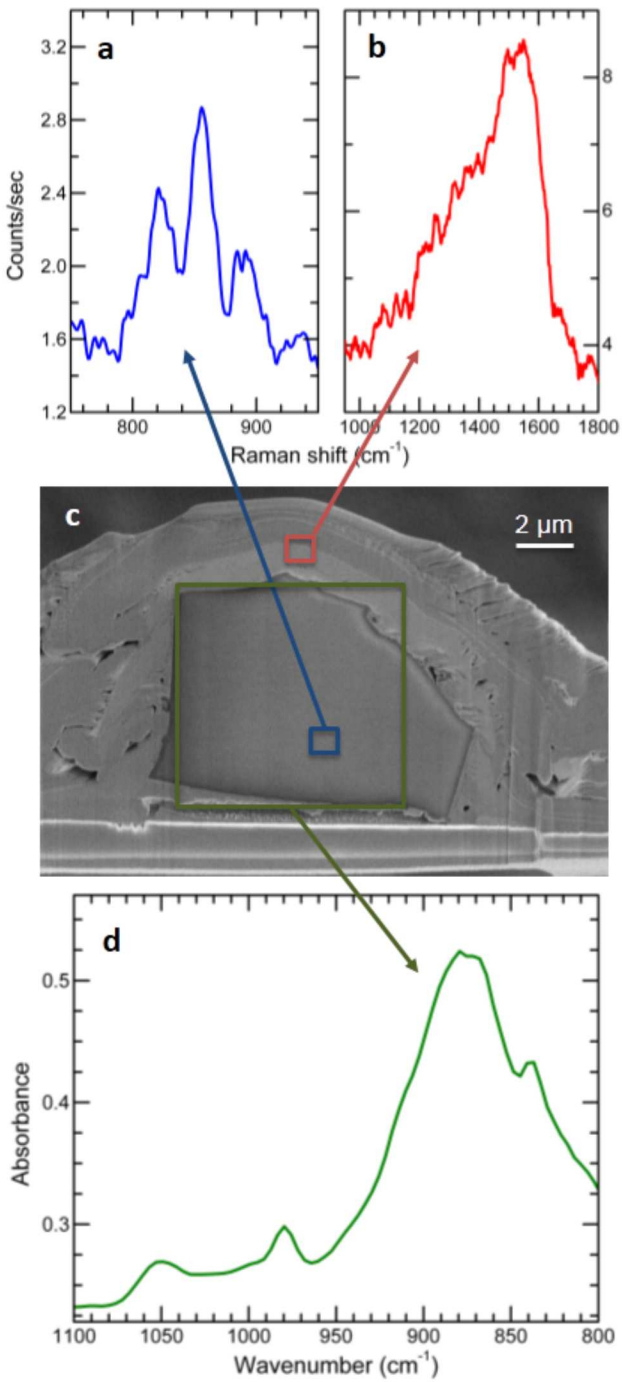
a
b
c
d
Counts/sec
Raman shift (cm-1)
2 µm
Absorbance
Wavenumber (cm-1)

FIG 6

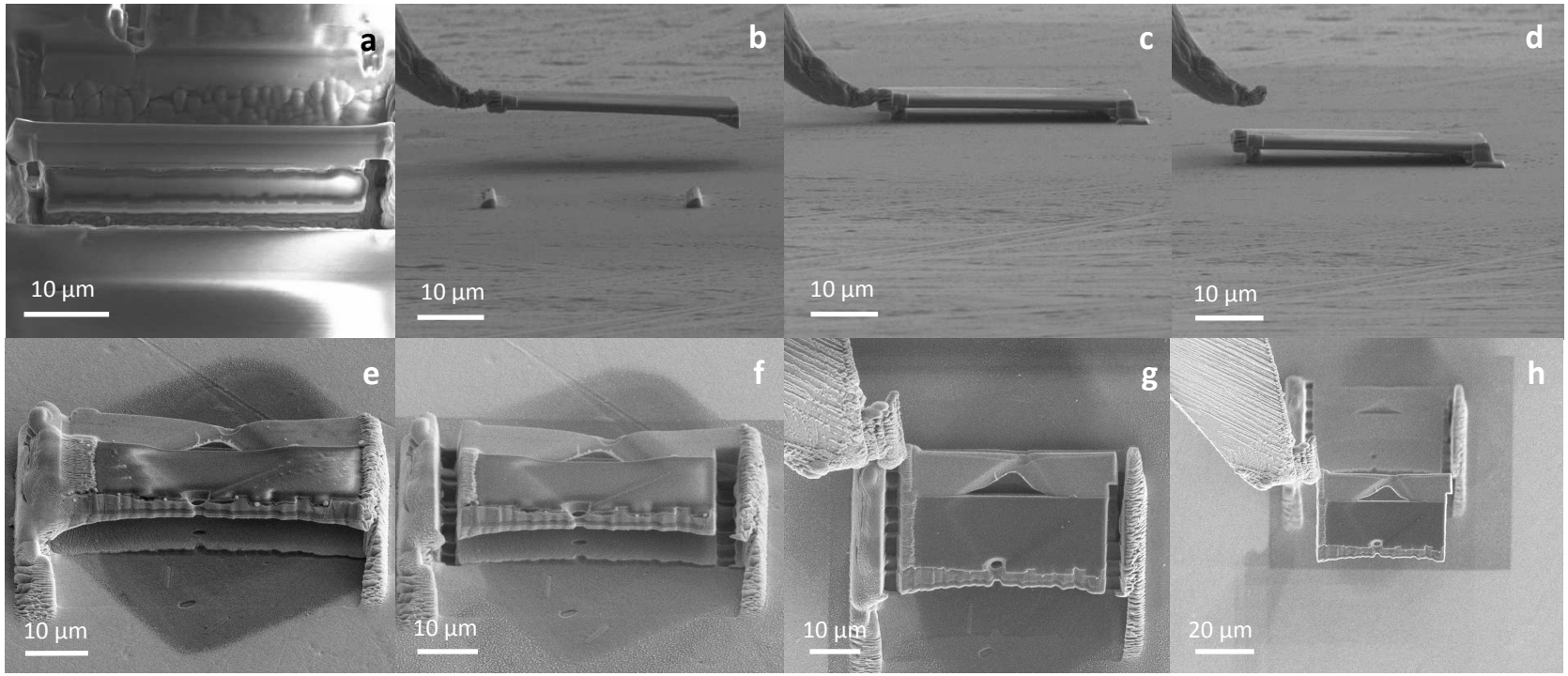

FIG 7

Fig. 8

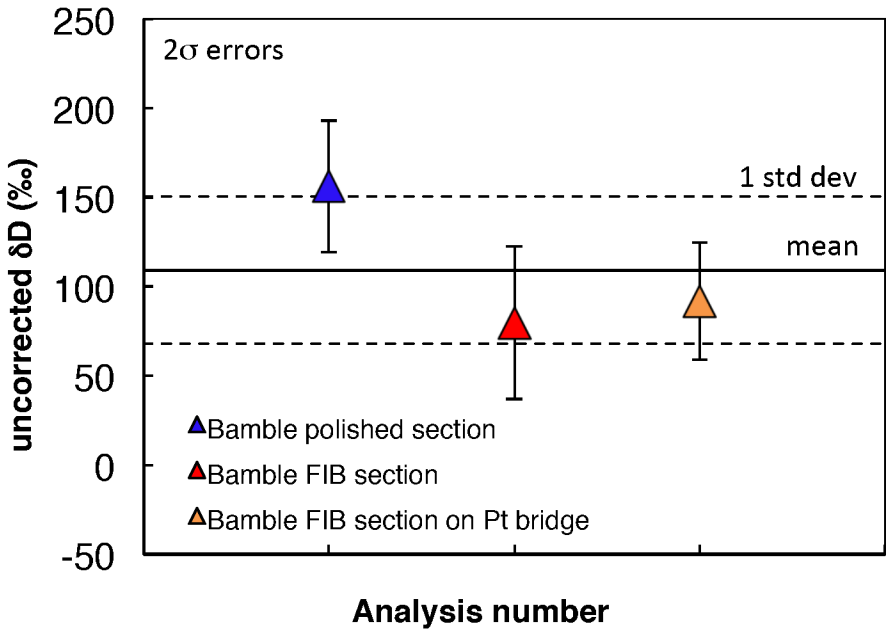
250
200
150
100
50
0
-50
2σ errors
1 std dev
mean
uncorrected δD (‰)
Bamble polished section
Bamble FIB section
Bamble FIB section on Pt bridge
Analysis number

FIG 8

Fig. 8

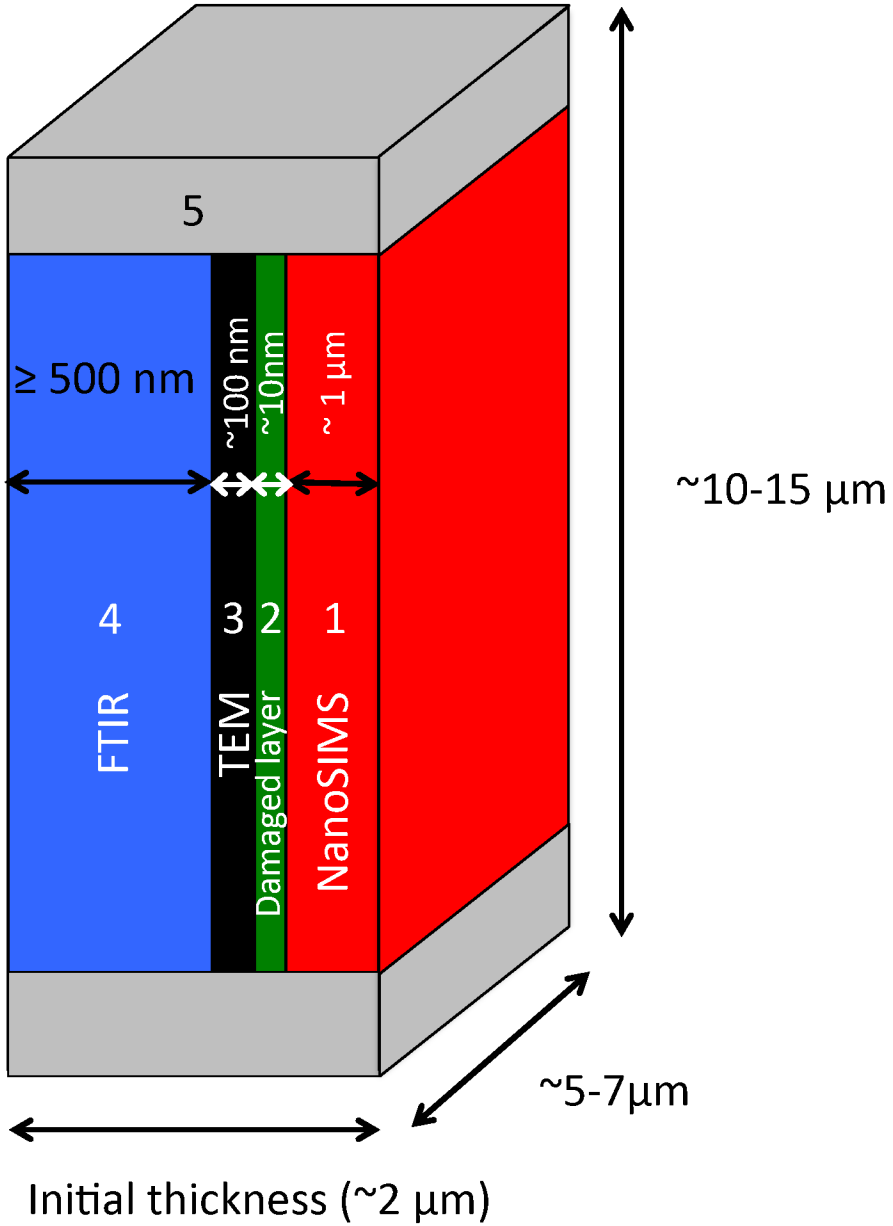
5
≥ 500 nm
~100 nm
~10nm
~ 1 µm
~10-15 µm
4
3
2
1
FTIR
TEM
Damaged layer
NanoSIMS
~5-7µm
Initial thickness (~2 µm)

FIG 9

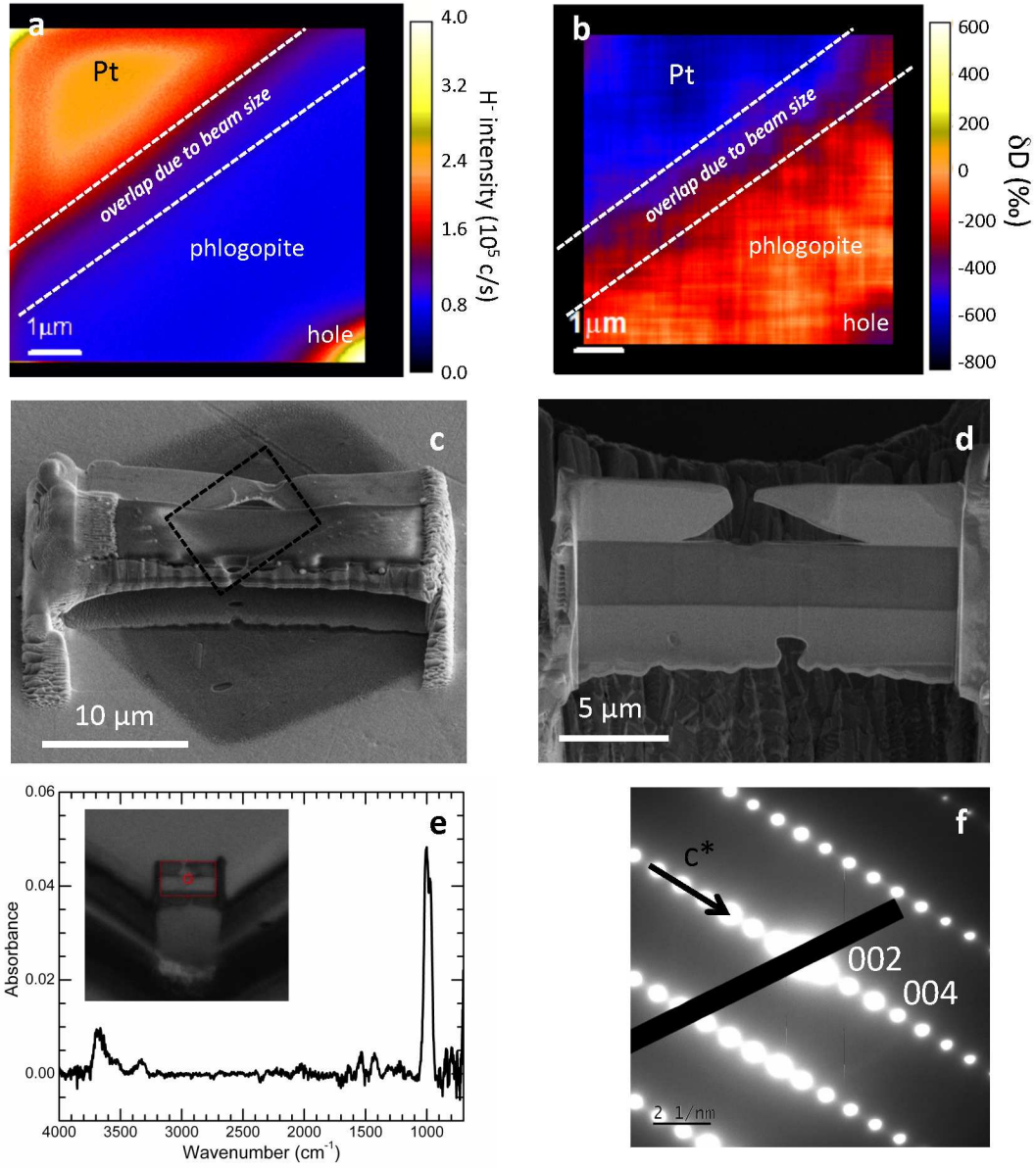
a
Pt
overlap due to beam size
phlogopite
1µm
hole
4.0
3.2
2.4
1.6
0.8
0.0
H- intensity (10^5 c/s)
b
Pt
overlap due to beam size
phlogopite
1µm
hole
600
400
200
0
-200
-400
-600
-800
δD (‰)
c
10 µm
d
5 µm
e
0.06
0.04
0.02
0.00
Absorbance
4000
3500
3000
2500
2000
1500
1000
Wavenumber (cm-1)
f
c*
002
004
2 1/nm

FIG. 10

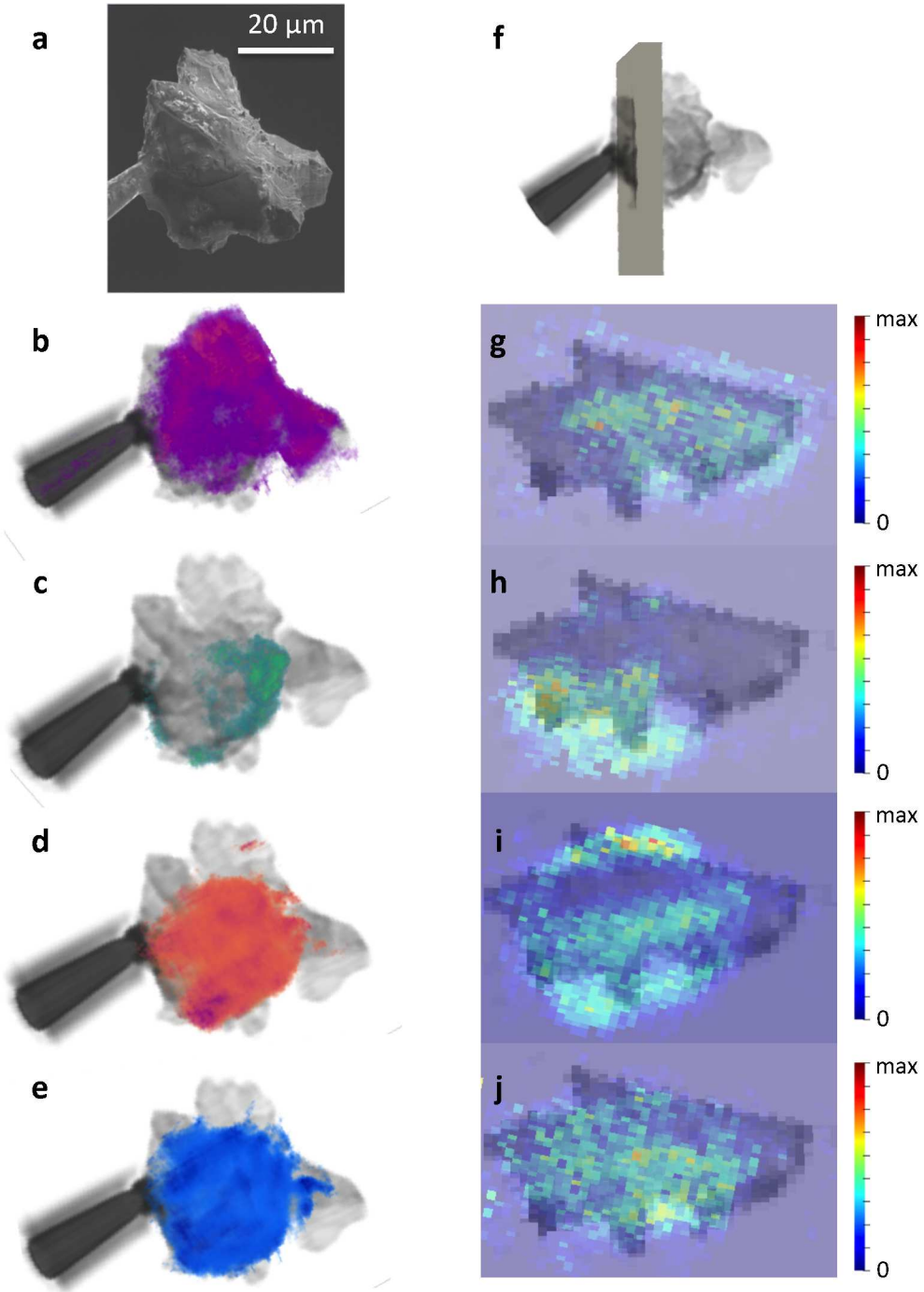

FIG. 11

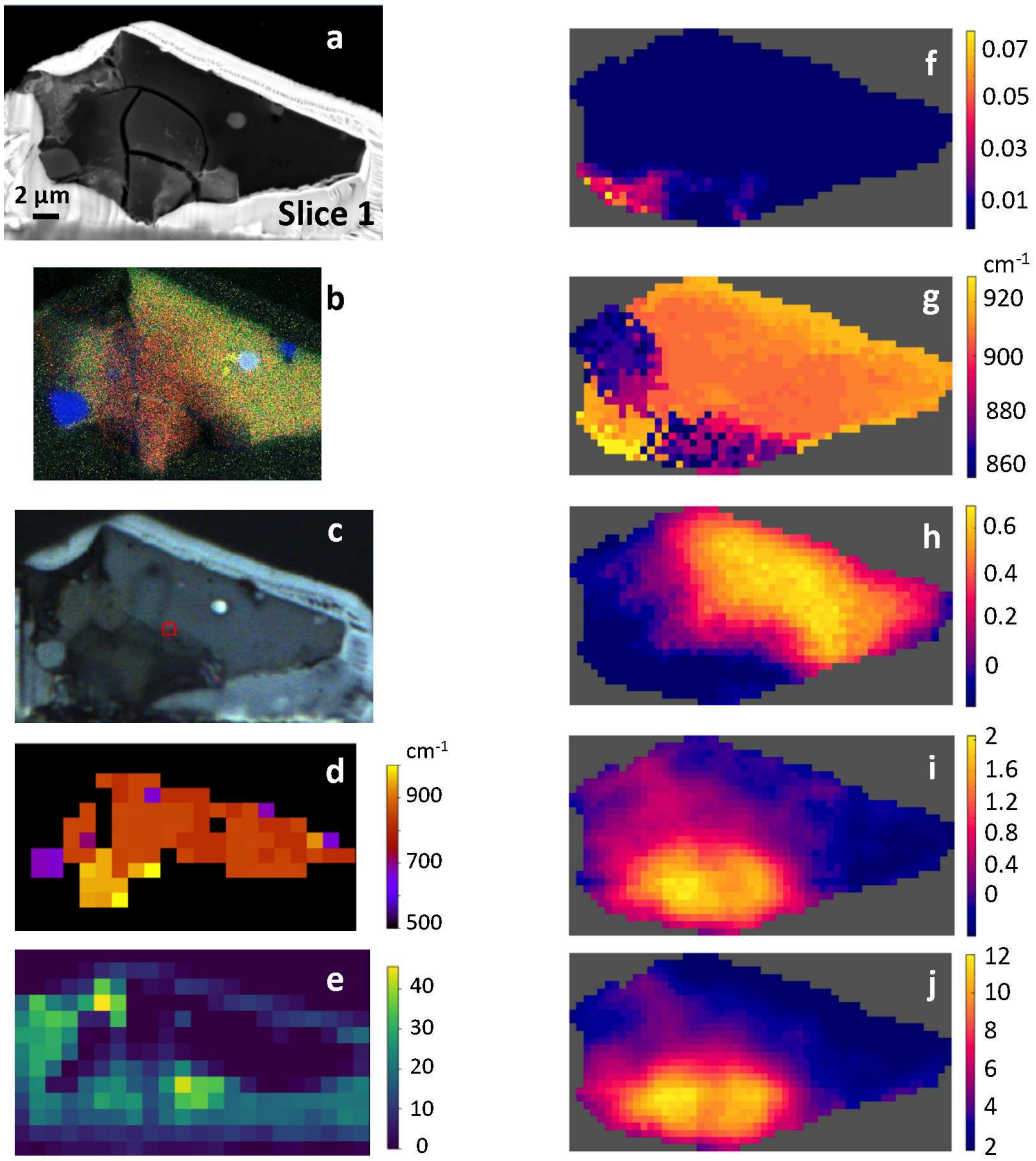
a
2 µm
Slice 1
b
c
d
cm-1
900
700
500
e
40
30
20
10
0
f
0.07
0.05
0.03
0.01
g
cm-1
920
900
880
860
h
0.6
0.4
0.2
0
i
2
1.6
1.2
0.8
0.4
0
j
12
10
8
6
4
2

FIG. 12

Fig. 13

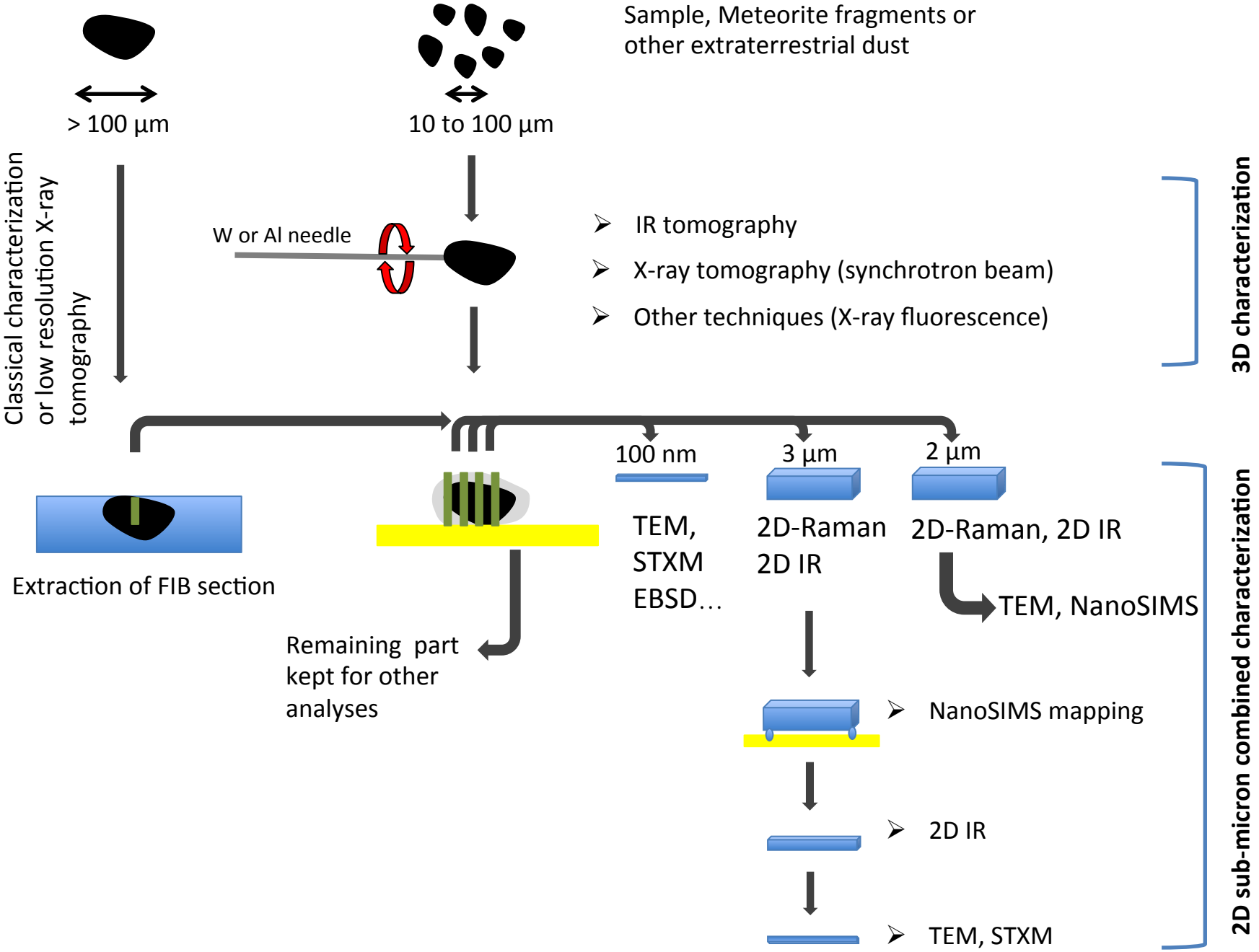
Sample, Meteorite fragments or other extraterrestrial dust
> 100 µm
10 to 100 µm
Classical characterization or low resolution X-ray tomography
W or Al needle
IR tomography
X-ray tomography (synchrotron beam)
Other techniques (X-ray fluorescence)
3D characterization
100 nm
3 µm
2 µm
Extraction of FIB section
TEM, STXM EBSD…
2D-Raman 2D IR
2D-Raman, 2D IR
TEM, NanoSIMS
Remaining part kept for other analyses
NanoSIMS mapping
2D IR
TEM, STXM
2D sub-micron combined characterization